Effect of Atomization Gas Properties on Droplet Atomization in an 'Air-Assist' Atomizer

by

Robert Aftel

Report submitted to the Faculty of the
Virginia Polytechnic Institute and State University
in partial fulfillment of the requirements for the degree of
Master of Engineering
in
Mechanical Engineering

APPROVED

Uri Vandsburger

Balakrishnan Ganeshan

May 1996

Blacksburg, Virginia

Keywords: Spray Combustion, Phase-Doppler Interferometry

Effect of Atomization Gas Properties on Droplet Atomization in an 'Air-Assist' Atomizer

by

Robert Aftel

Uri Vandsburger and Balakrishnan Ganeshan, Chairmen

Mechanical Engineering

(ABSTRACT)

Air, nitrogen, argon and carbon dioxide were used as the atomizing gas in an 'air-assist' spray nozzle to determine the effect of these gases on mean droplet size, number density, velocity and their distributions in kerosene fuel spays and spray flames using a two-dimensional phase Doppler interferometer. Data have been obtained with these atomizing gases using a base, air assisted case as a reference, since this is the most commonly used atomizing fluid in almost all applications. Comparisons were made between the gases on a mass and momentum flux basis. Both burning and nonburning sprays were investigated. The results show significant differences in atomization characteristics from the atomizer with different gases and under conditions of constant mass and momentum flux of the gas. The results also show that the presence of oxygen in the air atomized sprays assists in the combustion process, since it produces smaller and faster moving droplets, especially at locations near to the nozzle exit. In nonburning sprays, droplets had similar size and velocity. Lighter gases such as nitrogen more effectively atomized the fuel in comparison to the denser gases. Argon and carbon dioxide produced larger, slower moving droplets than air and nitrogen assisted cases in both the burning and nonburning sprays. Flame photographs revealed the argon and carbon dioxide atomized flames to have greater luminosity than air or nitrogen atomized flames.

ACKNOWLEDGMENTS

The author wishes to extend his gratitude to Dr. Uri Vandsburger for his guidance and support. Dr. Vandsburger's expertise as an experimentalist and his optical diagnostics skills made the work go more smoothly. Our spirited technical discussions made me feel prepared to take on any hostile conference audience. I just hope I wasn't responsible for the loss of too much of his hair.

At the National Institute for Standards and Technology (NIST), the assistance of Drs. Charles Cooke and Cary Presser is recognized. At the University of Maryland, the assistant of Joerg Schreck and Martin Bruegmann was indispensible for conducting the experiments and reducing the data.

Last, but certainly not meant to be the least, my wife Nora, for putting up with me whilst attempting to earn this degree. Hopefully, our lives will now settle down and be less stressful.

TABLE OF CONTENTS

LIST OF FIGURES

LIST OF TABLES

NOMENCLATURE

MMD	mass mean diameter
S	swirl number
U_R	relative velocity of atomization gas and fuel
m_L	mass flow rate of liquid fuel
m_A	mass flow rate of atomization gas
r	radial distance from spray centerline [mm]
z	axial distance from nozzle [mm]
ρ	density
ν	fuel viscosity

1.0 Introduction

The combustion of liquid fuels has been, and continues to be, an important area of combustion research. Given the multitude of applications for liquid fuels, and the ever pressing need for cleaner and more efficient combustion technologies, this area is likely to receive more attention in coming years.

Liquid fuels are typically atomized prior to combustion. This process increases the surface area of the fuel and allows it to combust more quickly and more cleanly. This is important in gas turbines or Diesel engines, where the space, and therefore time available for combusting the fuel is limited due to physical constraints on the combustors size. The atomization process breaks the liquid fuel into a multitude of small (~2-100 μm) droplets which are more easily (and cleanly) combusted. Several types of atomizers, or nozzles, exist to perform this task, and they fall into several groups (Lefebvre, 1989):

Pressure Atomizer: This atomizer is simple and cheap to assemble, and rugged in service environments. It employs high fuel pressure flowing through a narrow orifice to break up the fuel stream into droplets. The disadvantages of this nozzle are these narrow passages, which are prone to clogging and are ill-suited for high viscous fuels, and the narrow spray angle which develops, which hinders fuel/oxidizer mixing, lengthening the time needed for complete combustion of the droplets produced. High supply line pressures also necessitate the added complexity of high pressure fuel pumps and fuel lines. The atomization quality obtained from these atomizers deteriorates rapidly with decreaseing fuel flow rate because of the reduced fuel pressure differential across the nozzle orifice. These nozzles may be found most commonly in Diesel engines and gas turbines, where high fuel pressures may be easily obtained.

Air-Assist: This nozzle atomizes the fuel by directing a high velocity air (or steam) flow against the fuel. The transfer of flow energy from the air to the fuel breaks the fuel into

droplets. This design provides good atomization with a well dispersed spray (wide cone angle). It is clog resistant, and it atomizes highly viscous fuels well. Droplet characteristics may be modified independant of the fuel flow rate by modifing the rate of atomization gas flow. These nozzles may also simulate pressure jet nozzles in the absence of atomization gas. The main disadvantage of air-assist atomzers lies in the added complexity of supplying atomizing gas. These nozzles may be most commonly found in industrial furnaces.

Other general nozzle types include ultrasonic, which use high frequency acoustic energy to destabilize a liquid film into droplets and provide very fine atomization with a low droplet velocity, but cannot handle high flow rates. Electrostatic nozzles work by applying electrical pressure to the liquid film, which causes an expansion in the liquid film surface area. When these forces exceed the surface tension of the liquid, atomization occurs. These nozzles share these same advantages and disadvantages.

An Air-assist nozzle was chosen for study in this work. The purpose of this study was to investigate, using phase Doppler interferometry, the effect of N_2, Ar and CO_2, on the atomization of kerosene in an 'air-assist' atomizer. The objective was to determine if these gases can influence atomization as a result of their density or oxygen content. Table 1.1 gives a summary of the properties of the gases used. Several studies have been carried out on air-assisted atomization of liquids (Presser, et. al. 1988, Bulzan, 1993, Edwards, et. al. 1990), but little information exists on the advantages of using different gases other than air to influence spray flame characteristics.

Table 1.1 Properties of Selected Atomizing Gases

Gas (@STP)	Density (Kg/m^3)	Specific Heat c_p (KJ/Kg K)
Air	1.1614	1.007
N2	1.1233	1.041
Ar	1.602	0.5203
CO2	1.7730	0.851

In order to compare one gas with another, it was important to ensure that the various gases were metered properly. The atomization of liquid fuels within an 'air-assist' atomizer occurs due to the interaction of the fuel and atomization gas, and the controlling factors of this interaction had to be determined. Earlier works with air-assisted atomizers were always limited to a single atomization gas, and comparison between gases was difficult to make. Typically, the mass flow rate of the atomization gas was considered the controlling factor affecting the atomization process (Lefebvre, 1989). Given the same atomization gas, a given mass flow rate would yield a unique momentum and energy flow rate as well. A more comprehensive correlation of atomization gas flow and subsequent atomization was needed.

Wigg (1964) provided an empirical correlation that allowed for the fact that mass flux was not the only determining factor affecting droplet size in an air-assist atomizer. His correlation is dependent on mass flux, atomization gas density, and fuel/air relative velocity as follows:

$$MMD = 20\upsilon_L^{0.5}\dot{m}_L^{0.1}\left(1+\frac{\dot{m}_L}{\dot{m}_A}\right)^{0.5} h^{0.1}\sigma^{0.2}\rho_A^{-0.3}U_R^{-1.0} \qquad (1.1)$$

In the preceding equation, MMR indicates the predicted mean droplet diameter, ν indicates the viscosity of the fuel, m is the mass flow rate, h is the height of the air annulus within the atomizer, σ is the surface tension of the fuel, ρ the density, and U_R is the relative velocity of the liquid fuel and atomization gas. The subscripts L and A indicate properties for the fuel and atomization gas, respectively.

In the experiments performed, the fuel properties and flow rates were held constant, as was the atomizing nozzle used. This allowed the preceding expression to be simplified somewhat:

$$MMD \propto \left(1+\frac{\dot{m}_L}{\dot{m}_A}\right)^{0.5} \rho_A^{-0.3}U_R^{-1.0} \qquad (1.2)$$

This simplified expression indicates that the mean droplet sizes produced within a given air-assist atomizer using a given fuel are dependent on both the fuel and atomization gas mass flow rates, atomization gas density, and relative velocity of the atomization gas and the fuel. The mass flux of atomization gas may be expressed as $\rho_A U_A$, and the momentum flux by $\rho_A(U_A)^2$. If the density of the atomization gas is doubled while maintaining the mass flux constant, the flow velocity of the atomization gas will be halved. If we further assume further that $U_A \approx U_R$ (a good assumption in the case of an air-assist atomizer, where atomization gas velocities may be nearly sonic), it can be shown that the equation will predict that the droplets formed by a denser atomization gas flowing at the identical mass flow rate will be larger. In the case where the atomization gas is twice as dense as the baseline, droplet size is predicted to increase by 62% (see Appendix A) when the mass flow rate of the atomization gases are held constant. In the case where the momentum flux of the atomization gas is held constant, droplet sizes are predicted to be nearly equal (see Appendix A).

These results indicate that as atomizing gas velocity is increased, droplet size decreases. In order to maintain constant mass or momentum flux as gas density is increased, the atomizing gas velocity must decrease, and therefore increased droplet sizes are predicted.

Both nonburning and burning sprays were investigated while maintaining either the mass or momentum flux of the atomizing gas constant. Air was considered as the base line case. Since N_2 has a similar density to air, one case was carried out for N_2, representing both the mass and momentum controlled cases. Ar and CO_2 were examined separately under constant mass and momentum flux.

2.0 Experimental Apparatus

The burner assembly is a swirl burner with a changeable 12 vane swirl cascade, and is shown in Figure 2.1. The swirl vanes are adjusted simultaneously to meet the desired degree of swirl intensity for the combustion air flow. The swirl strength introduced to the combustion air is given in terms of the swirl number, S. The experiments discussed here have a swirl number of S = 0.3 (i.e. example in Appendix A). Combustion air passes through a 101 mm diameter pipe that surrounds the fuel nozzle. The fuel nozzle is fixed at

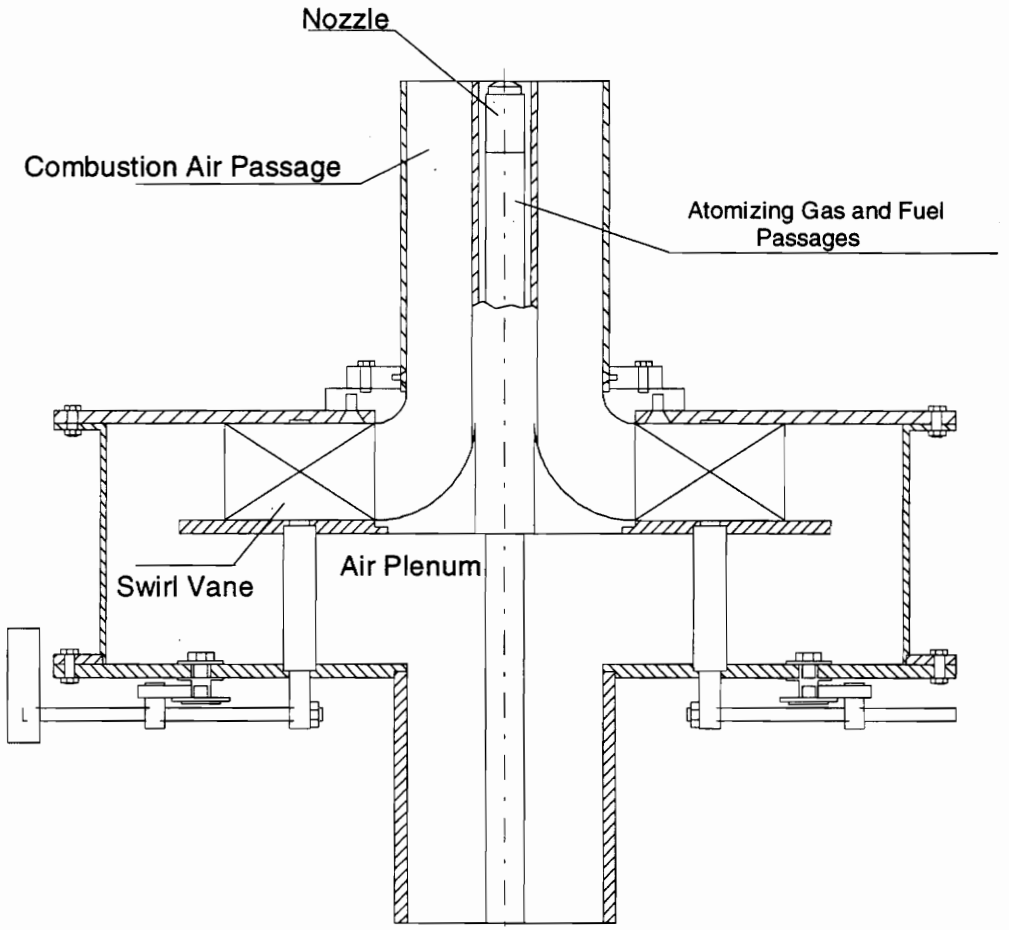

Figure 2.1: Swirl vane burner

the center of the combustion air passage. It supplies the fuel and the atomizing air through two different passages. All experiments discussed in this thesis were carried out using the

commercial air atomizing nozzle, type 30609-11 SNA 1.00, produced by Delavan Inc., shown in Figure 2.2. Air, or any other gas (e.g., N_2, Ar or CO_2), can be used as the atomizing fluid of the fuel. This readily interchangeable air assist atomizing fuel nozzle provides a nominal 45° solid cone unconfined kerosene spray, which is injected vertically upwards from the nozzle exit.

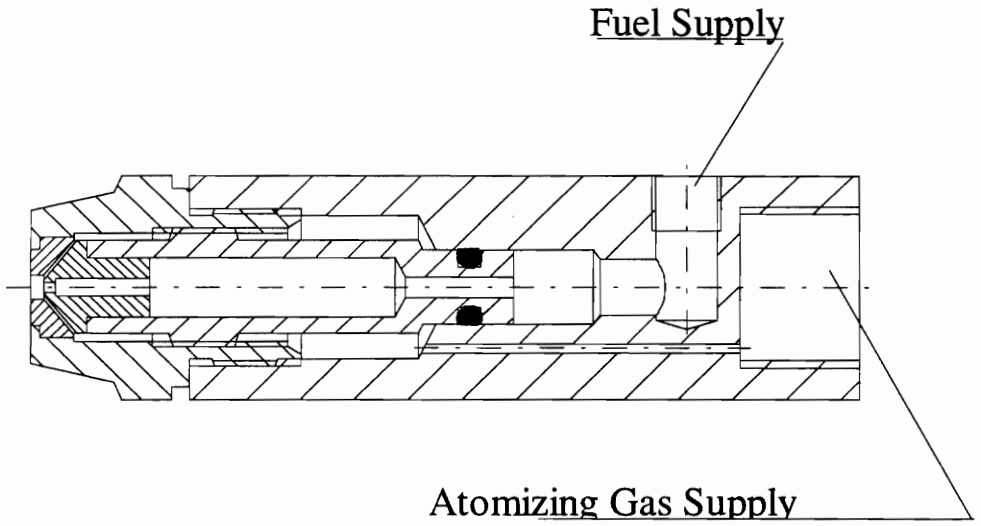

Figure 2.2: Air-atomizing nozzle, type 30609-11 SNA 1.00 produced by Delavan Inc.

In these experiments, kerosene was supplied at a rate of 4.1 kg/h. The atomizing gas was introduced through a surrounding annulus and swirled within the nozzle. In the mass flow controlled cases, the mass flow rate of the atomizing gas (air, N_2, Ar or CO_2) was set to 1.64 kg/h. In the momentum controlled case, the momentum flux was set to 7.86×10^{-2} kg/m·h^2. Combustion air flow in all cases was set to 210 kg/h, over two orders of magnitude greater than the atomizing gas flow. This provided an inlet equivalence ratio of approximately 0.29 (see calculation in Appendix A).

In the nonburning experiments, a propane fueled afterburner placed 60 cm downstream of the spray nozzle, was used to burn the fuel droplets before they entered the exhaust duct.

A two-component phase Doppler interferometer (PDI) (Bachalo, et. al., 1984) was used to determine fuel droplet size, number density and velocity, in both burning and nonburning sprays. The data rates were determined as discussed in Presser, et. al. (1994). Results were repeatable within a 5% margin for mean particle size, axial velocity and number density. Global features of the spray and spray flame were obtained using direct photography.

2.1 Traverse Assembly

The swirl vane burner was mounted on a three-dimensional traversing assembly. The traverse provided controlled movement in the vertical (Z) direction and both horizontal (X and Y) directions. The swirl burner could move a distance of 380 mm in the vertical Z direction (with a resolution of 0.05 mm) and 200 mm in the horizontal X direction (with a resolution of 0.01 mm). Movement in each direction was provided by stepper motor controlled translation stages. A manual translation stage, having a limited range of ± 25.4 mm (with a resolution of 0.01 mm) about the burner axis in the horizontal Y direction, enabled precise alignment of the burner assembly with the surrounding optical equipment. The optical equipment was fixed in position and could move independently about the spray and traversing assembly, thus eliminating the need to readjust or realign the optics at each spatial point of the spray flame. The burner was placed under a fumehood to allow the disposal of the combustion products. The configuration of the burner and its additional facilities is shown in Figure 2.3, viewed from above.

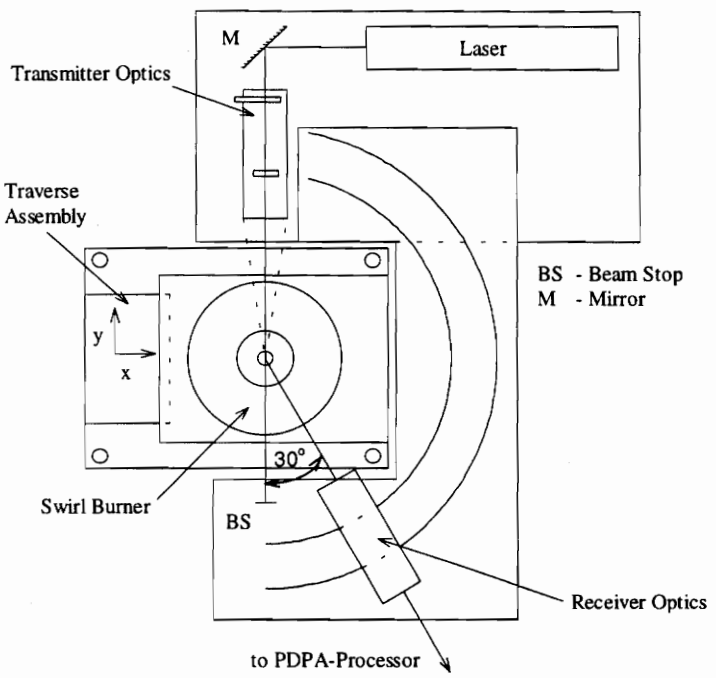

Figure 2.3: Schematic of the experimental droplet velocity/sizing apparatus

2.2 Phase Doppler Particle Analyzer

A 4 W argon-ion laser (Spectra Physics) operating at a wavelength of 514.5 nm was fixed on the laser table and placed perpendicular to the burner. The laser was part of the PDI system which is described below. The method, as illustrated in Figure 2.4 and in Appendix B, utilizes an optical system which is the similar to that required for a conventional LDV system, except that three detectors are located at selected well-known spacings behind the receiver aperture.

Durst and Zaré (1975) have shown that the phase angle of a Doppler burst from a particle varies depending on the position at which the signal is collected and the size of the particle. If light scattered from a spherical particle is collected at two different locations in space, the phase difference between the signals will be directly proportional to the size of the particle. These three detectors of our system provide simultaneous measurements of

two components (axial and radial) of the droplet velocity. The signals of two detectors are compared with the signal of the third one.

The theory and application of this technique are described by several authors (Durst, et. al., 1975, Bachalo, et. al. 1984) and are explored in some detail in Appendix B.

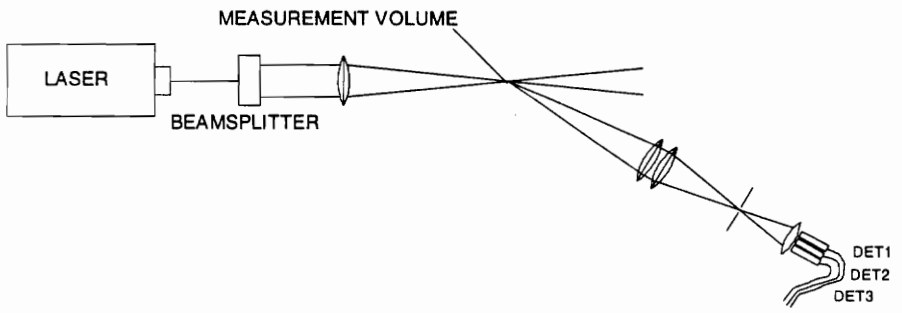

Figure 2.4: Optical Schematic of the PDI

The PDI system used was version 4.27j produced by Aerometrics Inc., and consisted of six major components: transmitter, receiver, signal processor, motor controller box and computer. This system incorporated and extended the particle velocity measurement ability of a conventional laser Doppler Velocimeter (LDV) with the addition of particle sizing capabilities. Spherical particles ranging in diameter from 0.5 μm to over 3000 μm could be measured over a dynamic range of 100 μm at a single optical setting.

At the same time, particle velocities up to 100 m/s could be measured depending on the particle size range and optical setup. For the experiments discussed here the diameter range was set at 2 μm to 100 μm. The settings for the velocities varied depending on the position being measured within the spray. The optical transmitting system was designed to generate four equal intensity laser beams of two colors and focus them on an intersection point which created the probe volume. Optical components within the transmitter serve to focus, partition, and collimate the laser beam. A combination of three

output lenses provided a satisfactory beam intersection angle. It should be noted that the particle velocity is very sensitive to the fringe spacing and in this way also to the intersection angle.

Inside of the transmitter, the laser beam is split into two colors, a blue (488 nm) beam and a green (514 nm) one. The beamsplitter is a radial diffraction grating which has three separate tracks to give three different beam separations. It is driven by a high speed DC motor. Rotation of the grating produces a frequency differential between the diffracted beams which is used to create a frequency shift on measured particle signals. The two beams are then split into four beams, which are focused into the probe volume, which is about 1 mm^3 in size. A motor controller box controls both the grating motor and the track select motor. Scattered light was collected using off-axis light-collection optics positioned at a scattering angle of 30°. Because prior experiments have been performed on this burner facility, both a suitable collimating lens (focal length 300 mm by 90 mm diameter) and a suitable output lens (focal length 500 mm by 90 mm diameter) were already installed.

The controller software for the entire PDI system was operated with a Gateway 486-66 PC. The computer controlled the operational parameters of the PDI system including PMT voltage, as well as sensitivity ranges for droplet size and velocity. Once the system components were physically set up and aligned, parameters could be set by the software to automate data collection and signal reduction. Real time data collection and display provided statistical features such as Sauter mean diameter (D_{32}), mean axial velocity (U_{mean}), mean radial velocity (V_{mean}), number density (ND), arithmetic mean diameter (D_{10}), rms of axial velocity (rmsu), and rms of radial velocity (rmsv). Rejected data points and their causes (PMT saturation, particles falling outside of predetermined size or velocity ranges) were also displayed, aiding in system optimization. On-line display on the screen of histograms of each component (D, U_{mean}, V_{mean}) was also very helpful to

optimize the system settings. After a run the software created a data file (ASCII) with all droplet properties for each droplet of the sample, if desired.

2.3 Sample Spray Photographs

Figures 2.5 and 2.6 display a photographs of a sample nonburning and burning spray. The photographs of the nonburning spray were obtained by directing the 514 nm light from the argon laser through a set of cylindrical lenses to create a sheet of light, which was directed across the nozzle and illuminated the droplets as they were ejected from the nozzle.

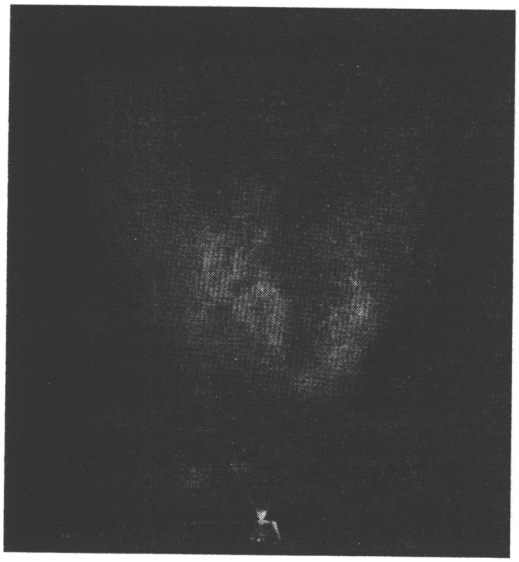

Figure 2.5 Nonburning Spray(Presser, et. al., 1993)

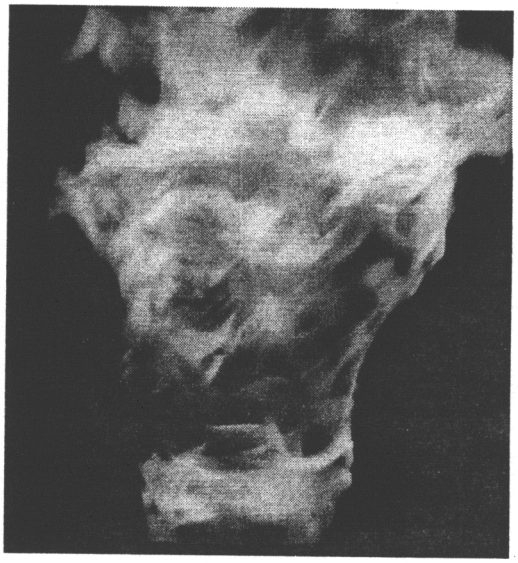

Figure 2.6 Burning Spray (Presser, et. al. 1993)

3.0 Results

The initial objective of this work was to determine what effect, if any, the density and heat capacity of the atomizing gas has on the properties of the droplets formed. There was some doubt as to whether any effect would be observed - atomization gas flow rates are typically less than 1% of the total oxidizer flow rate.

Each flame was photographed to obtain a qualitative assessment of the quality of combustion. Flame height and luminosity were observed to change when different atomization gases were used. Phase-Doppler interfereometry was used to obtain information on the droplet parameters. Sauter mean diameter, axial velocity, number density and fuel flux are reported here for all the burning and nonburning sprays investigated.

Since the sprays were axisymmetric (Presser, et. al. 1989), droplet size, velocity and number density were measured with the PDI from the spray centerline to the edge of the spray, in increments of 1.27 mm at an axial position (z) of 10 mm downstream from the nozzle, and increments of 2.54 mm at z = 15, 20, 25, 30, 35, 40, 50 and 60 mm. Results for z = 10 and 50 mm are presented in order to describe the salient features of axial distance on droplet properties.

3.1 Experimental Observations

The different cases (i.e., air, N_2, Ar and CO_2 for constant mass and momentum control) were photographed to record the global flame features and were used to aid in the interpretation of the PDI measurements. Light from an argon laser was formed into a sheet with cylindrical optics and directed along the centerline of the nozzle to illuminate the droplets. All of the photographs shown were exposed identically to eliminate any differences in appearance due to exposure time or aperture. It was observed that the flame front for the reference, air-assisted spray

flame extended upstream along the core of the spray flame, see Fig. 3.1. No other flame showed flame penetration into the core of the spray flame. The observed flame height and luminosity for air were reduced in comparison to the other flames, illustrating the effect of increased O_2 availability. The N_2 atomized flame (Fig. 3.2) appeared similar to the air atomized flame, except that the flame front did not penetrate as close to the nozzle. Instead, the flame stood off the nozzle by about 5 cm. The unburned droplets in this area can be seen in the photograph as a light gray area between the nozzle and the flame. Flame height and luminosity increased for the other atomizing gases in the following order: N_2 (Fig. 3.2), Ar (Figs. 3.3 and 3.5) and CO_2 (Figs 3.4 and 3.6). This illustrated the effect of increasing atomizing gas density on reducing droplet vaporization and combustion in the region downstream of the nozzle where the atomizing gas was most influential. Strong differences may be seen in the mass and momentum controlled cases of Ar and CO_2. In the mass controlled Ar case (Fig. 3.3), the flame stands off about 5 cm above the nozzle. The area between the nozzle and the flame front appears nearly black in the photograph - fewer droplets are present, and they do not scatter much light from the laser. When the flow rate of Ar is momentum controlled, the stand off distance of the flame remains similar, but the droplets become visible. Similar effects may be noted for the CO_2 atomized flames (Fig. 3.4 and 3.6).

3.2.1 Nonburning Sprays - Mass Flux Controlled

Measured droplet Sauter mean diameters and axial velocities in the nonburning sprays are presented in Figs. 3.7 and 3.8. Frames 'a' and 'c' of each figure present results for mass flux controlled atomization, while 'b' and 'd' denote momentum flux controlled atomization. In the nonburning spray, the effect of gas density may be separated from that of heat capacity, which does not play a role in nonburning

sprays. This allows for investigation of gas density effects on droplet atomization in the absence of any chemical or thermal effects.

The results presented in Figs. 3.7 and 3.8 indicate that mean droplet size and velocity are affected by atomizing gas density. The influence of the gas density is most significant in the region where the atomizing gas is encountered, i.e., near the spray centerline and at axial positions near the nozzle. At the spray centerline and at z = 10 mm (see Fig. 3.7.a and Table 3.1), atomizing air produced droplets with a Sauter mean diameter of 25.5 μm, while N_2 formed droplets with a 20.6 μm diameter. Droplets formed in the Ar and CO_2 atomized sprays were considerably larger, at 29.2 and 30.0 μm, respectively. The difference in size between the smallest and largest droplets at this location was 9.4 μm, and it was observed that the Ar and CO_2 atomized sprays had a considerably wider size distribution, with a σ on the order of 9, as opposed to air and N_2, which had a σ of 7. As seen in Fig. 3.7.a, the droplet size produced by the air atomized spray on centerline at z = 10 mm is anomalous - on centerline, the droplets produced by the air spray are almost 5 μm larger than those produced in the N_2 spray, while at other locations at the z = 10 elevation, the diameters are nearly identical. This result was expected based on the fact that densities of air and N_2 are similar. At a radial distances of 9 mm (near the spray boundary, Table 3.2), all the gases produce similar mean droplet sizes (within 3 μm), demonstrating the overriding influence of main combustion air in this region.

At z = 50 mm and the spray centerline (Fig. 3.7.c), the mean droplet diameter for atomizing air was 18.7 μm, N_2 was 18.4 μm, Ar was 20.9 μm, and CO_2 was 20.2 μm, a difference of 2.4 μm from smallest to largest. Differences between the sprays are reduced at this elevation, as the effects of the surrounding main combustion air become more dominant at the spray centerline.

Similar differences are noted for the axial velocity results shown in Fig. 3.8.a, where air and N_2 droplets have the greatest velocities on the spray centerline at z = 10 mm (19.1 and 18.9 m/s, respectively), followed by Ar (15.9 m/s) and CO_2 (13.1 m/s). These differences remain pronounced at the spray centerline and z = 50 mm (Fig. 3.8.c), with air and N_2 atomized droplets having the largest velocities (11.4 and 10.2 m/s, respectively), followed by Ar (4.6 m/s) and CO_2 (3.3 m/s). At greater radial or axial distances from the nozzle (Table 3.6), the effect of the surrounding combustion air on droplet velocity becomes dominant. This result is expected from the fact that the surrounding combustion air (and other operating conditions) remained unchanged between experiments.

Measured droplet number densities for the nonburning mass controlled sprays are shown in Fig. 3.9.a,c. There are few droplets near the spray centerline, which is typical for a full cone spray. The greatest density of droplets occurs near r = 9 mm, defined here as the spray boundary. In the mass flow controlled case at z = 10 mm (Fig. 3.9.a), air and N_2 produce the highest number density of droplets, peaking near 8000 droplets/cm^3. The actual number density of droplets is likely to be higher than that figure, since the reported number density does not account for signals rejected by the PDI system software, which can be up to 30% of the signal received. Ar and CO_2 produced lower droplet number densities, peaking at about 7000 droplets/cm^3.

At z = 50 mm, the position of the number density peak, with the exception of N_2, moves to the spray centerline. The trend established at z = 10 mm is also inverted, with CO_2 and Ar atomized sprays now producing the highest number density of droplets.

The fuel volumetric flux for the nonburning mass controlled sprays is shown in Fig. 3.10. In all cases investigated, burning and nonburning, mass and momentum controlled, the fuel flow rate was kept constant at 4.1 kg/h. The fuel volumetric flux rate, expressed here in cm^3/s, determines the flow rate of fuel in a given area. Since the total fuel input is constant, this measure can give a determination of how well the spray disperses the droplets, since a more dispersed spray will have an overall lower volumetric flux (same amount of fuel spread over a wider area). In burning sprays, it can also account for droplet vaporization and combustion. Unfortunately, it is also the most error laden measurement shown here. The volumetric flux rate is dependent on the droplet diameter, which is well known, and the droplet number density, which is prone to error, as discussed earlier. In the measurements shown here, typical validation rates were on the order of 70%. This indicates that around 30% of the droplets entering the probe volume are ignored. Therefore, this data can only be taken to describe qualitative trends, and should not be taken at its absolute values.

The fuel volumetric flux for nonburning, mass controlled sprays at z = 10 mm is shown in Fig. 3.9.a, and is typical for a full-cone air-assist nozzle. Most of the fuel flows through a ring between 9 and 13 mm from the centerline of the spray. There is little fuel flowing at the centerline, or the edge of the spray. This result was expected since an air-assist full cone atomizer was used. At this elevation, the spray is evolving, and still under the influence of the atomization gas. CO_2 produces the highest peak flux, 1.5×10^{-5} cm^3/s near the spray boundary. Air and Ar produce a peak flux of 1.2×10^{-5} cm^3/s, followed by N_2 with 1.1×10^{-5} cm^3/s.

At z = 50 mm, the volumetric flux is reduced - the spray spans a wider area here, and the droplets have dispersed and/or partially vaporized. Since the data rate and validation rate were reduced at this elevation, the resulting data has more scatter.

CO_2 and Ar atomized sprays persist in having a higher volumetric flux, followed by N_2 and then air. This indicates that the droplets produced in the N_2 and air atomized sprays were more evenly dispersed at this elevation.

3.2.2 Nonburning Sprays - Momentum Flux Controlled

Momentum flux controlled sprays produced smaller (see Fig. 3.7.b,d), higher axial velocity (Fig. 3.8.b,d) droplets compared with the mass flux controlled sprays. As in the mass flow controlled cases, air produced the largest droplets on the spray centerline at z = 10 mm (25.5 μm). N_2 produced droplets with a mean diameter of 20.6 μm, followed by Ar (22.7 μm), and CO_2 (24.6 μm), giving a difference of 4.9 μm between the smallest and largest droplets at that position. With the exception of the previously mentioned anomaly in the data obtained for air at that centerline position, denser atomization gases continued to produce larger droplets when metered to produce identical momentum fluxes, although the differences were reduced in comparison to the mass controlled case. Also apparent in Table 3.1 is the fact that the width of the droplet distributions is more similar in the momentum controlled cases than in the mass controlled cases, with typical distribution widths on the order of 7 μm.

Near the spray boundary (r = 9 mm) there is little difference in droplet diameter between the momentum controlled cases, with a maximum difference of only 2 μm between the smallest and largest droplets at the location (see Table 3.2). At the spray edge, the differences are similarly reduced (Table 3.3). It is interesting to note the change in the width of the droplet size distribution with radial position - moving from the centerline to the spray edge, this parameter doubles. Near the spray edge, the influence of the intensely turbulent, swirling main combustion air is more strongly felt, and this widens the size distribution of the droplets.

Differences in droplet size are still significant at z = 50 mm, with the momentum controlled gases producing droplets with mean sizes within 4 μm of each other. Moving towards the spray edge reduces these differences, but increases the width of the size distribution, as previously stated.

Velocity data are presented in Fig. 3.8.b,d. On the spray centerline and at z = 10 mm, air and N_2 assisted droplets had a velocity of 19.1 and 18.9 m/s, respectively. Ar assisted droplets had a velocity of 18.2 m/s, and CO_2 assisted droplets had a velocity of 17.6 m/s, a difference of only 1.5 m/s between the fastest and slowest droplets at that position. Droplet axial velocities for all the momentum controlled sprays remain similarly uniform throughout the elevation. At z = 50 mm, CO_2 (11.9 m/s) droplets have the highest velocity, followed by N_2 (11.4 m/s), Ar (11.1 m/s), and air (10.2 m/s), a difference of only 1.7 m/s between the fastest and slowest droplets. From these results, it is apparent that nearly identical droplet velocities can be produced with atomization gases of differing densities by ensuring that the momentum flux of the atomization gases are held to a constant value.

Droplet number density for the momentum controlled nonburning sprays is shown in Fig. 3.9.b,d. With the exception of Ar, the droplet number densities are similar for all the atomization gases used at z = 10 mm, and peak near the spray boundary (r = 9). At z = 50, droplet number densities are strongly reduced, and peak near the spray centerline.

Fuel volumetric flux for the nonburning momentum controlled sprays at z = 10 mm is shown in Fig. 3.10.b. Compared with the data for the mass controlled case shown in Fig. 3.9.a, it is apparent that the differences in flux between the various atomization gases are reduced in the momentum controlled case. At z = 50 mm, Ar and CO_2 atomized sprays appear to have better dispersion, with lower

volumetric fluxes than the air or N_2 atomized sprays. This is the inverse of what was observed in the mass controlled cases (Fig. 3.9.c).

3.3.1 Burning Sprays - Mass Flux Controlled

Results for droplet Sauter mean diameter, axial velocity, number density and fuel volumetric flux for the burning sprays are presented in Figs. 3.11-3.14. With combustion, the effect of atomizing gas density and heat capacity on droplet atomization and vaporization are coupled. Comparing the mass flow controlled cases at z = 10 mm in Fig. 3.10.a, air and N_2 assisted sprays produce droplets with mean sizes of 27.8 and 25.7 μm (Table 3.7), respectively while Ar and CO_2 atomized sprays produce the largest droplets at the spray centerline (30.2 and 28.7 μm, respectively). As seen in the nonburning case, the droplet size distributions are wider in the Ar and CO_2 atomized cases.

On the spray boundary at z = 9 mm, air and N_2 producing droplets with a Sauter mean diameter of 19.9 μm and 16.4 μm, compared with 18.1 μm and 21.5 μm in the Ar and CO_2 assisted flames. In the burning cases investigated, the atomizing gases have their greatest influence on droplet diameter near the spray boundary. Droplet diameter in the air atomized case is strongly increased in comparison to N_2, whereas it was nearly identical in the nonburning cases (Fig. 3.7, Table 3.2).

Figure 3.11.a shows that the air assisted sprays have the highest velocity at z = 10 mm near the center of the spray (19.1 m/s). N_2 atomized droplets have a velocity of 19.3 m/s, while Ar and CO_2 atomized droplets are slower at 17.0 and 14.8 m/s respectively. Near the spray edge at the same axial distance, the velocity difference between the fastest and the smallest droplets is reduced to only 0.9 m/s (Table 3.9).

At z = 50 mm (Fig. 3.10.c), Ar and CO_2 atomized flames have consistently larger droplets from the centerline to the spray edge (Tables 3.9-3.12). At z = 50 mm and the spray centerline (Fig. 3.10.c), droplets in the air assisted case remain the fastest (8.1 m/s), followed by N_2 (8.0 m/s), Ar (7.9 m/s) and CO_2 (6.7 m/s). At the spray edge, the velocity difference between the fastest and smallest droplets at z = 50 is reduced to 0.4 m/s.

Number density results for the mass flow controlled burning sprays are shown in Fig. 3.13,a,c. Air produces the highest peak number density of droplets at z = 10 mm and the spray boundary, with approximately 10000 droplets/cm^3, followed by N_2 with approximately 8000 droplets/cm^3, Ar with 6000 droplets/cm^3, and CO_2 with 3000 droplets/cm^3. For all case, at z = 50 mm (see Fig. 3.13c), droplet combustion and evaporation have significantly reduced the droplet number density, and the position of the peak number density has moved to the spray centerline, as in the nonburning case. CO_2 produces a peak number density at this axial distance of 850 droplets/cm^3. N_2 produces nearly 800 droplets/cm^3 at the centerline, and Ar produces less than 500 droplets/cm^3. The droplets atomized by air have the lowest number density, at less than 400 droplets/cm^3.

Fuel volumetric flux for the mass flux controlled cases at z = 10 mm is shown in Fig. 3.13.a. The air atomized spray generally has the lowest volumetric flux, except in the region near the spray boundary (r = 9 mm), where its volumetric flux is the highest. N_2 and Ar have fairly similar volumetric fluxes which peak near the spray boundary, while CO_2 atomized sprays have the lowest volumetric flux.

At z = 50 mm, the trend is reversed, with CO_2 atomized flames having the highest volumetric fluxes, followed by Ar, N_2 and air. It is also interesting to note that the position of peak volumetric flux has shifted from the spray boundary to the spray

centerline. This occurs due to the fact that main combustion air must convect and/or diffuse a greater distance to combust droplets on the spray centerline. This results in fewer droplets evaporating or combusting on centerline. The air atomized flame has the lowest volume flux, especially in comparison to N_2. This is due to the chemical participation of the oxygen within the atomization air in the combustion process. This results in larger, faster droplets at low elevations, and fewer droplets at higher elevations. Fuel volume flux is lower in the air-atomized cases because there are fewer droplets available.

3.3.2 Burning Sprays - Momentum Flux Controlled

At z = 10 mm near the centerline of the spray (see Fig 3.10.b, Table 3.7), air-atomized sprays produced droplets with a mean diameter of 27.8 μm, while N_2 produced droplets of 25.7 μm, Ar produced droplets of 26.6 μm and CO_2 produced the smallest droplets at 22.3 μm. Droplet velocities (see Fig. 3.11.b, Table 3.7) remained high for air (19.1 m/s), followed by N_2 (19.3 m/s), Ar (18.3 m/s), and CO_2 (16.1 m/s). Near the spray edge, these differences disappear and the droplets have similar velocities regardless of the atomizing gas used.

At z = 50 mm (see Fig. 3.10.d), air-atomized droplets are the largest at 24.9 μm, followed by N_2 (22.4 μm). Droplets produced by Ar atomization are slightly larger (23.5 μm) than those produced by CO_2 (22.7 μm). As shown in Fig. 3.11.d and Table 3.10, air-atomized droplets have the greatest velocity (8.1 m/s), followed by N_2 and Ar (8.0 m/s), while CO_2 droplets were slightly slower (7.2 m/s). Differences in droplet velocity between cases remain small at all other radial positions at this elevation, since droplet behavior is more influenced by the surrounding combustion air at these positions. Air-atomized flames produce the largest droplets since all of the smaller droplets have been vaporized or combusted by the time the droplets reach this elevation, leaving only larger droplets.

Droplet number densities for the burning momentum flux controlled cases are shown in Fig. 3.13.b,d. Air atomization produced droplet number densities in excess of 10000 droplets/cm^3 at z = 10 mm and at the spray boundary. CO_2 and N_2 peaked at approximately 8000 droplets/cm^3, and Ar peaked at approximately 6000 droplets/cm^3. At z = 50 mm, CO_2 produces the highest density of droplets at the centerline (over 1000 droplets/cm^3), followed by Ar (850 droplets/cm^3), N_2 (750 droplets/cm^3) and air (400 droplets/cm^3). At this point, any available O_2 in the atomizing air has likely been consumed. Droplet number densities are lowest on the spray edge due to the availability of combustion air to vaporize and combust the droplets.

Fuel volumetric flow rate of the momentum controlled burning sprays is shown in Fig. 3.13.b,d. In comparison to the mass controlled cases shown in Fig. 3.13.a,c, the differences between the various atomization gases are reduced, but the trends seen in the mass controlled cases remain. At z = 10 mm (Fig. 3.13.b), most of the fuel flow is directed through the spray boundary between r = 8 and 13 mm. Air atomized flames have the highest volumetric flux, followed by CO_2, N_2 and Ar.

With the exception of the noted O_2 effects in the air atomized case, it is clear from the results that matching the momentum fluxes of the atomizing gases minimized differences in droplet size and velocity. This suggests that momentum, and not mass flux is a determining factor in droplet formation.

Table 3.1 Droplet Properties on Centerline at z = 10 mm

Atomization Gas	Sauter Mean Diameter ±σ (μm)	Axial Velocity ±σ (m/s)	Fuel Volume Flux (cm^3/s)
Air	25.5 ± 7.7	19.1 ± 5.3	1.5×10^{-7}
N_2	20.6 ± 6.4	18.9 ± 5.2	1.0×10^{-7}
Ar (mass controlled)	29.2 ± 9.2	15.9 ± 4.3	3.3×10^{-7}
Ar (momentum controlled)	22.7 ± 7.5	18.2 ± 5.1	9.1×10^{-8}
CO_2 (mass controlled)	30.0 ± 9.5	13.1 ± 4.1	4.6×10^{-7}
CO_2 (momentum controlled)	24.6 ± 7.4	17.6 ± 5.0	1.4×10^{-7}

Table 3.2 Droplet Properties on Spray Boundary (r = 9 mm) at z = 10 mm

Atomization Gas	Sauter Mean Diameter ±σ (μm)	Axial Velocity ±σ (m/s)	Fuel Volume Flux (cm^3/s)
Air	17.7 ± 6.7	6.4 ± 6.4	8.7×10^{-6}
N_2	16.8 ± 6.4	7.2 ± 4.8	7.7×10^{-6}
Ar (mass controlled)	20.6 ± 8.1	6.2 ± 4.4	9.6×10^{-6}
Ar (momentum controlled)	18.7 ± 6.9	7.0 ± 4.5	6.7×10^{-6}
CO_2 (mass controlled)	20.1 ± 7.9	5.7 ± 4.3	1.3×10^{-5}
CO_2 (momentum controlled)	18.4 ± 7.1	6.7 ± 4.5	9.8×10^{-6}

Table 3.3 Droplet Properties on Spray Edge at z = 10 mm

Atomization Gas	Sauter Mean Diameter ±σ (μm)	Axial Velocity ±σ (m/s)	Fuel Volume Flux (cm^3/s)
Air	43.4 ± 14.4	5.6 ± 2.2	2.4×10^{-6}
N_2	42.6 ± 13.8	5.8 ± 2.4	2.2×10^{-6}
Ar (mass controlled)	46.6 ± 15.7	5.9 ± 1.9	1.9×10^{-6}
Ar (momentum controlled)	42.0 ± 13.8	5.5 ± 2.2	1.8×10^{-6}
CO_2 (mass controlled)	48.9 ± 16.9	5.3 ± 1.6	2.2×10^{-6}
CO_2 (momentum controlled)	42.5 ± 13.4	5.4 ± 2.2	2.6×10^{-6}

Table 3.4 Droplet Properties on Centerline at z = 50 mm

Atomization Gas	Sauter Mean Diameter ±σ (μm)	Axial Velocity ±σ (m/s)	Fuel Volume Flux (cm^3/s)
Air	18.7 ± 6.5	10.2 ± 4.6	7.2×10^{-7}
N_2	18.4 ± 6.4	11.4 ± 4.4	9.9×10^{-7}
Ar (mass controlled)	20.9 ± 7.8	4.6 ± 3.9	2.3×10^{-6}
Ar (momentum controlled)	20.5 ± 7.1	11.1 ± 4.4	8.0×10^{-7}
CO_2 (mass controlled)	20.2 ± 8.0	3.3 ± 0.5	2.6×10^{-6}
CO_2 (momentum controlled)	19.4 ± 6.6	11.9 ± 4.1	6.4×10^{-7}

Table 3.5 Droplet Properties on Spray Boundary (r = 13 mm) at z = 50 mm

Atomization Gas	Sauter Mean Diameter ±σ (μm)	Axial Velocity ±σ (m/s)	Fuel Volume Flux (cm^3/s)
Air	18.6 ± 6.9	7.5 ± 2.8	7.5×10^{-7}
N_2	17.6 ± 6.4	7.8 ± 2.5	9.7×10^{-7}
Ar (mass controlled)	20.9 ± 8.0	3.9 ± 3.4	1.6×10^{-7}
Ar (momentum controlled)	20.5 ± 7.4	7.8 ± 2.9	7.3×10^{-7}
CO_2 (mass controlled)	20.6 ± 7.9	3.4 ± 3.0	1.6×10^{-6}
CO_2 (momentum controlled)	19.5 ± 7.2	8.1 ± 2.5	6.5×10^{-7}

Table 3.6 Droplet Properties on Spray Edge at z = 50 mm

Atomization Gas	Sauter Mean Diameter ±σ (μm)	Axial Velocity ±σ (m/s)	Fuel Volume Flux (cm^3/s)
Air	40.2 ± 12.7	5.9 ± 0.8	1.3×10^{-7}
N_2	36.5 ± 11.2	6.1 ± 0.8	1.3×10^{-7}
Ar (mass controlled)	39.8 ± 12.5	5.9 ± 0.8	1.9×10^{-6}
Ar (momentum controlled)	37.3 ± 11.5	6.1 ± 0.8	1.2×10^{-7}
CO_2 (mass controlled)	47.0 ± 15.4	6.0 ± 0.8	1.2×10^{-6}
CO_2 (momentum controlled)	39.5 ± 11.9	6.1 ± 0.9	8.5×10^{-8}

Table 3.7 Droplet Properties on Centerline at z = 10 mm

Atomization Gas	Sauter Mean Diameter ±σ (μm)	Axial Velocity ±σ (m/s)	Fuel Volume Flux (cm^3/s)
Air	27.8 ± 11.1	19.1 ± 6.1	8.3×10^{-7}
N_2	25.7 ± 8.1	19.3 ± 5.8	1.1×10^{-7}
Ar (mass controlled)	30.2 ± 9.5	17.0 ± 5.6	2.7×10^{-7}
Ar (momentum controlled)	26.6 ± 8.4	18.3 ± 5.5	2.3×10^{-8}
CO_2 (mass controlled)	28.7 ± 8.8	14.8 ± 4.4	2.1×10^{-7}
CO_2 (momentum controlled)	22.3 ± 7.1	16.1 ± 4.9	2.0×10^{-7}

Table 3.8 Droplet Properties on Spray Boundary (r = 9 mm) at z = 10 mm

Atomization Gas	Sauter Mean Diameter ±σ (μm)	Axial Velocity ±σ (m/s)	Fuel Volume Flux (cm^3/s)
Air	19.9 ± 7.0	7.0 ± 5.4	8.5×10^{-6}
N_2	16.4 ± 6.4	5.7 ± 5.0	7.8×10^{-6}
Ar (mass controlled)	18.1 ± 7.3	5.2 ± 5.1	8.5×10^{-6}
Ar (momentum controlled)	17.3 ± 7.0	5.7 ± 5.0	7.1×10^{-6}
CO_2 (mass controlled)	21.5 ± 8.3	7.0 ± 5.3	5.9×10^{-6}
CO_2 (momentum controlled)	17.0 ± 6.8	5.8 ± 4.9	8.8×10^{-6}

Table 3.9 Droplet Properties on Spray Edge at z = 10 mm

Atomization Gas	Sauter Mean Diameter ±σ (μm)	Axial Velocity ±σ (m/s)	Fuel Volume Flux (cm^3/s)
Air	43.2 ± 8.2	425 ± 5.6	2.9×10^{-7}
N_2	43.1 ± 15.6	4.7 ± 2.2	1.1×10^{-6}
Ar (mass controlled)	38.7 ± 14.8	4.0 ± 2.3	8.7×10^{-7}
Ar (momentum controlled)	44.6 ± 16.8	4.5 ± 2.2	7.3×10^{-7}
CO_2 (mass controlled)	40.3 ± 14.1	3.8 ± 2.1	9.0×10^{-7}
CO_2 (momentum controlled)	38.2 ± 14.7	3.9 ± 2.3	1.1×10^{-6}

Table 3.10 Droplet Properties on Centerline at z = 50 mm

Atomization Gas	Sauter Mean Diameter ±σ (μm)	Axial Velocity ±σ (m/s)	Fuel Volume Flux (cm^3/s)
Air	24.9 ± 9.2	8.1 ± 4.1	5.1×10^{-7}
N_2	22.4 ± 8.1	8.0 ± 3.7	7.8×10^{-7}
Ar (mass controlled)	26.5 ± 9.4	7.9 ± 3.4	7.7×10^{-7}
Ar (momentum controlled)	23.5 ± 8.2	8.0 ± 3.3	8.9×10^{-7}
CO_2 (mass controlled)	25.7 ± 9.3	6.7 ± 3.0	1.3×10^{-6}
CO_2 (momentum controlled)	22.7 ± 8.0	7.2 ± 3.4	8.3×10^{-7}

Table 3.11 Droplet Properties on Spray Boundary (r = 13 mm) at z = 50 mm

Atomization Gas	Sauter Mean Diameter ±σ (μm)	Axial Velocity ±σ (m/s)	Fuel Volume Flux (cm^3/s)
Air	28.5 ± 11.7	6.6 ± 4.1	2.9×10^{-7}
N_2	23.8 ± 8.9	6.2 ± 3.5	3.5×10^{-7}
Ar (mass controlled)	29.8 ± 11.3	6.1 ± 3.2	2.9×10^{-7}
Ar (momentum controlled)	26.4 ± 9.6	6.4 ± 3.3	3.3×10^{-7}
CO_2 (mass controlled)	33.8 ± 11.6	5.5 ± 2.8	7.6×10^{-8}
CO_2 (momentum controlled)	25.5 ± 9.2	5.8 ± 3.3	4.1×10^{-7}

Table 3.12 Droplet Properties on Spray Edge at z = 50 mm

Atomization Gas	Sauter Mean Diameter ±σ (μm)	Axial Velocity ±σ (m/s)	Fuel Volume Flux (cm^3/s)
Air	42.7 ± 14.6	6.0 ± 1.0	3.0×10^{-8}
N_2	34.2 ± 11.0	6.2 ± 1.0	4.0×10^{-8}
Ar (mass controlled)	38.1 ± 12.9	6.3 ± 1.1	3.7×10^{-8}
Ar (momentum controlled)	35.4 ± 12.0	6.1 ± 0.9	4.1×10^{-8}
CO_2 (mass controlled)	38.5 ± 13.1	6.1 ± 1.0	4.2×10^{-8}
CO_2 (momentum controlled)	36.5 ± 12.1	5.9 ± 0.9	5.5×10^{-8}

Figure 3.1: Burning air-atomized spray.

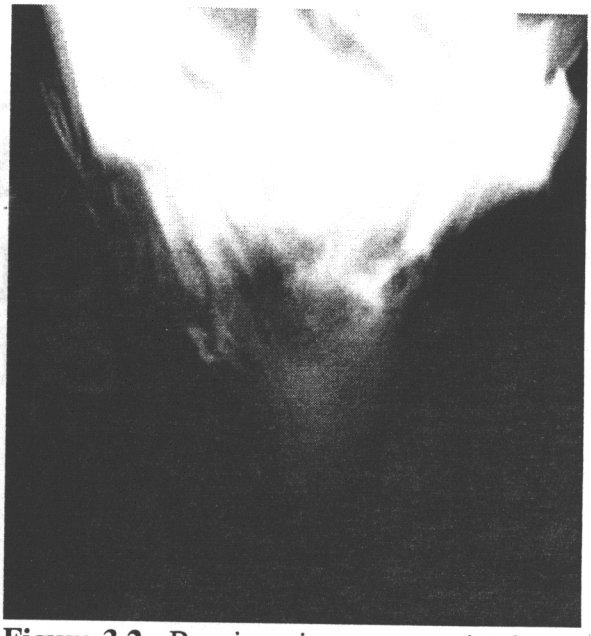

Figure 3.2: Burning nitrogen-atomized spray.

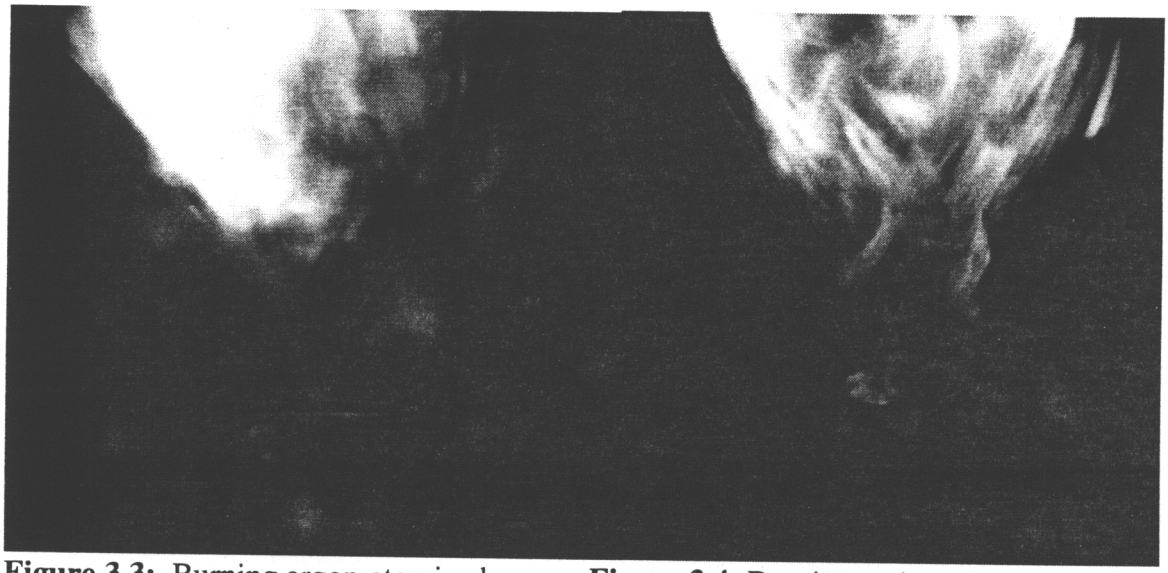

Figure 3.3: Burning argon-atomized spray (mass controlled).

Figure 3.4: Burning carbon-dioxide-atomized spray (mass controlled).

Figure 3.5: Burning argon-atomized spray (momentum controlled).

Figure 3.6: Burning carbon dioxide-atomized spray (momentum controlled).

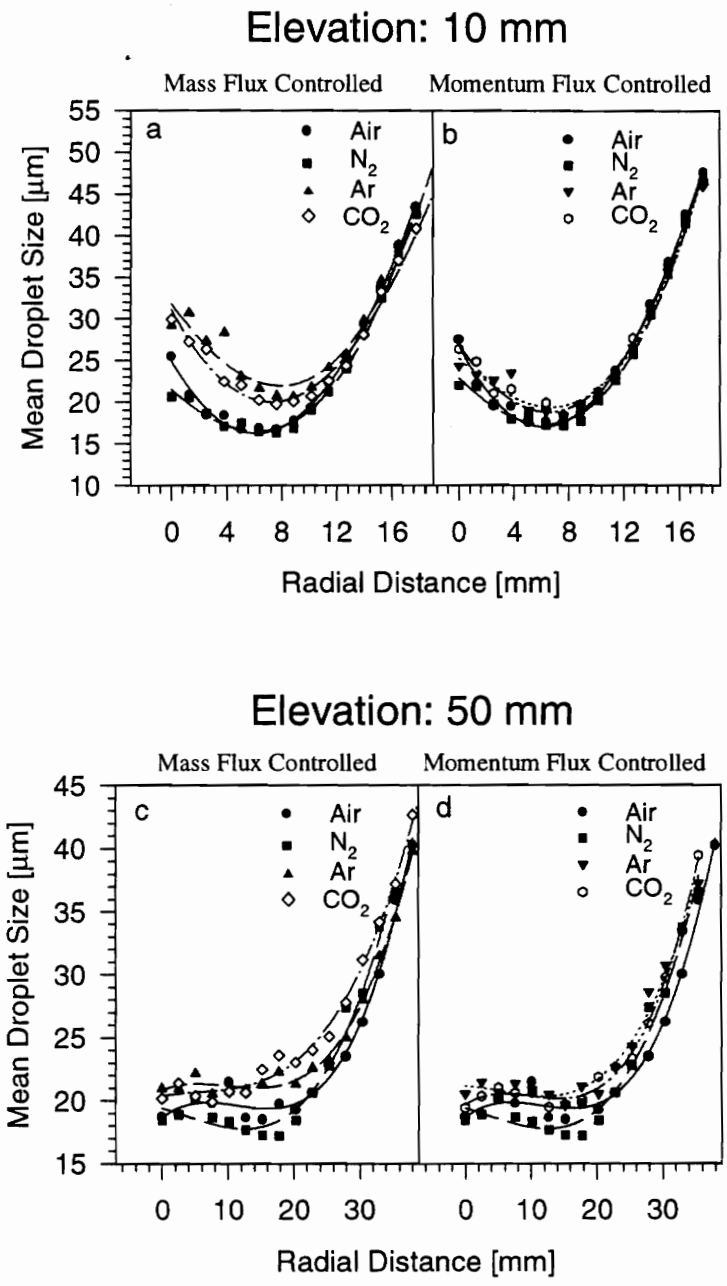

Figure 3.7: Sauter mean droplet size [µm] in nonburning sprays. (a) mass flow constant, z = 10 mm, (b) momentum flux constant, z = 10 mm, (c) mass flux constant, z = 50 mm, (d) momentum flux constant, z = 50 mm.

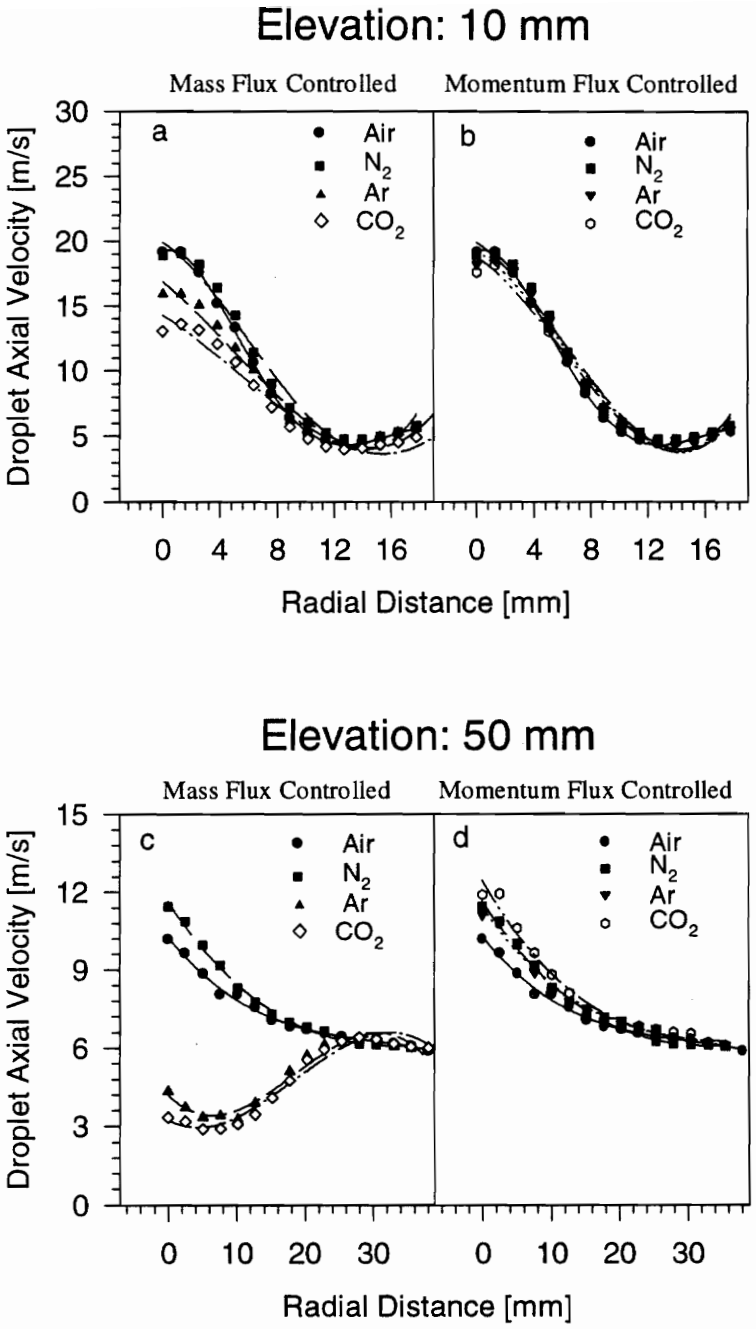

Figure 3.8: Axial droplet velocity [m/s] in nonburning sprays. (a) mass flow constant, z = 10 mm, (b) momentum flux constant, z = 10 mm, (c) mass flux constant, z = 50 mm, (d) momentum flux constant, z = 50 mm.

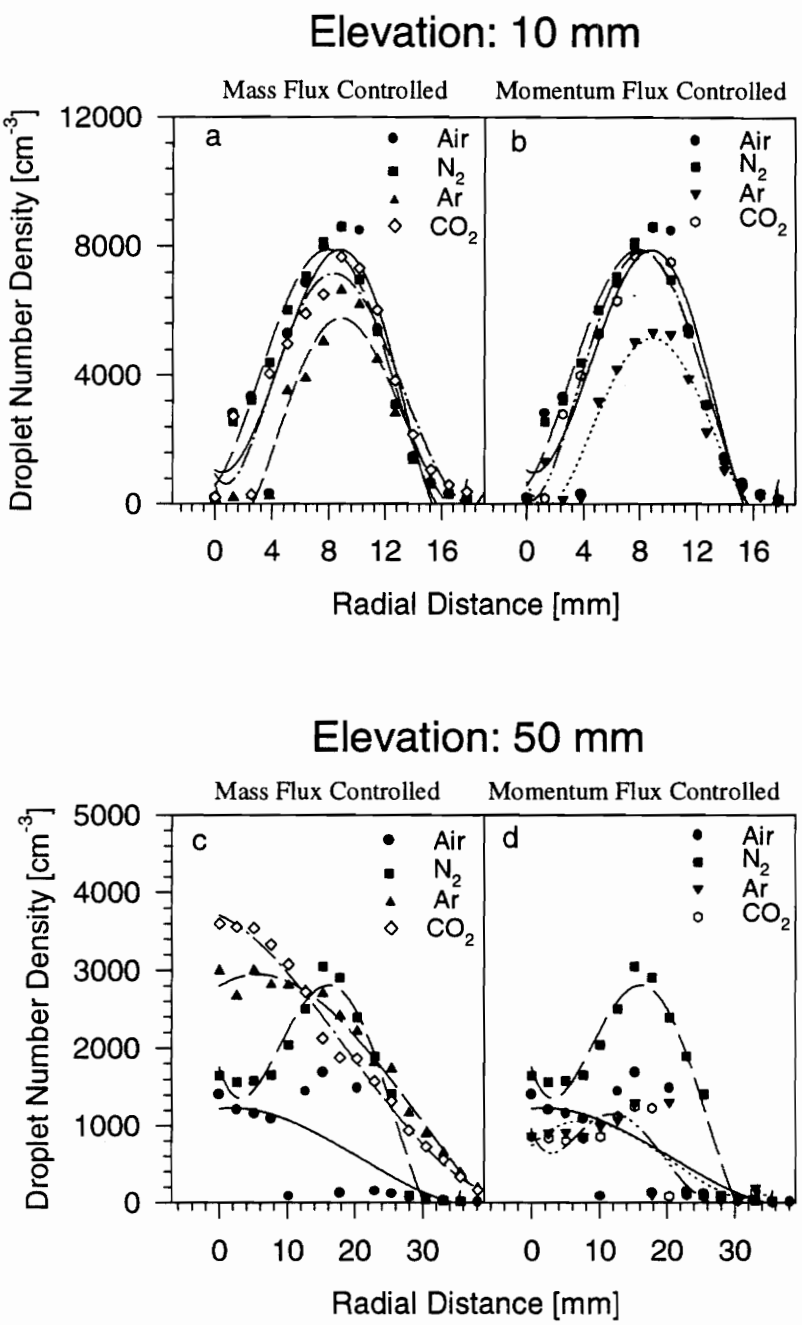

Figure 3.9: Droplet number density [Droplets/cm^3] in nonburning sprays. (a) mass flow constant, z = 10 mm, (b) momentum flux constant, z = 10 mm, (c) mass flux constant, z = 50 mm, (d) momentum flux constant, z = 50 mm.

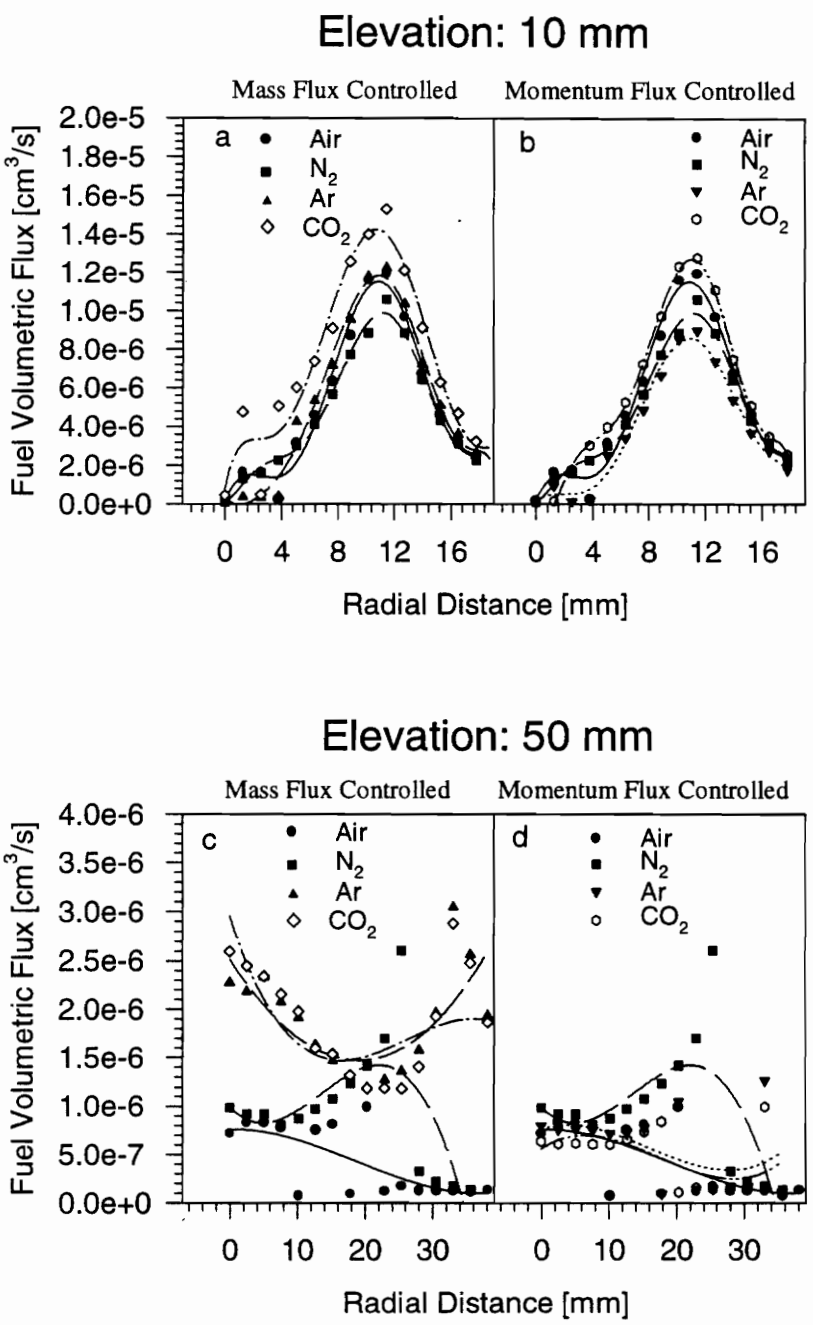

Figure 3.10: Fuel volumetric flux [cm^3/s] in nonburning sprays. (a) mass flow constant, z = 10 mm, (b) momentum flux constant, z = 10 mm, (c) mass flux constant, z = 50 mm, (d) momentum flux constant, z = 50 mm.

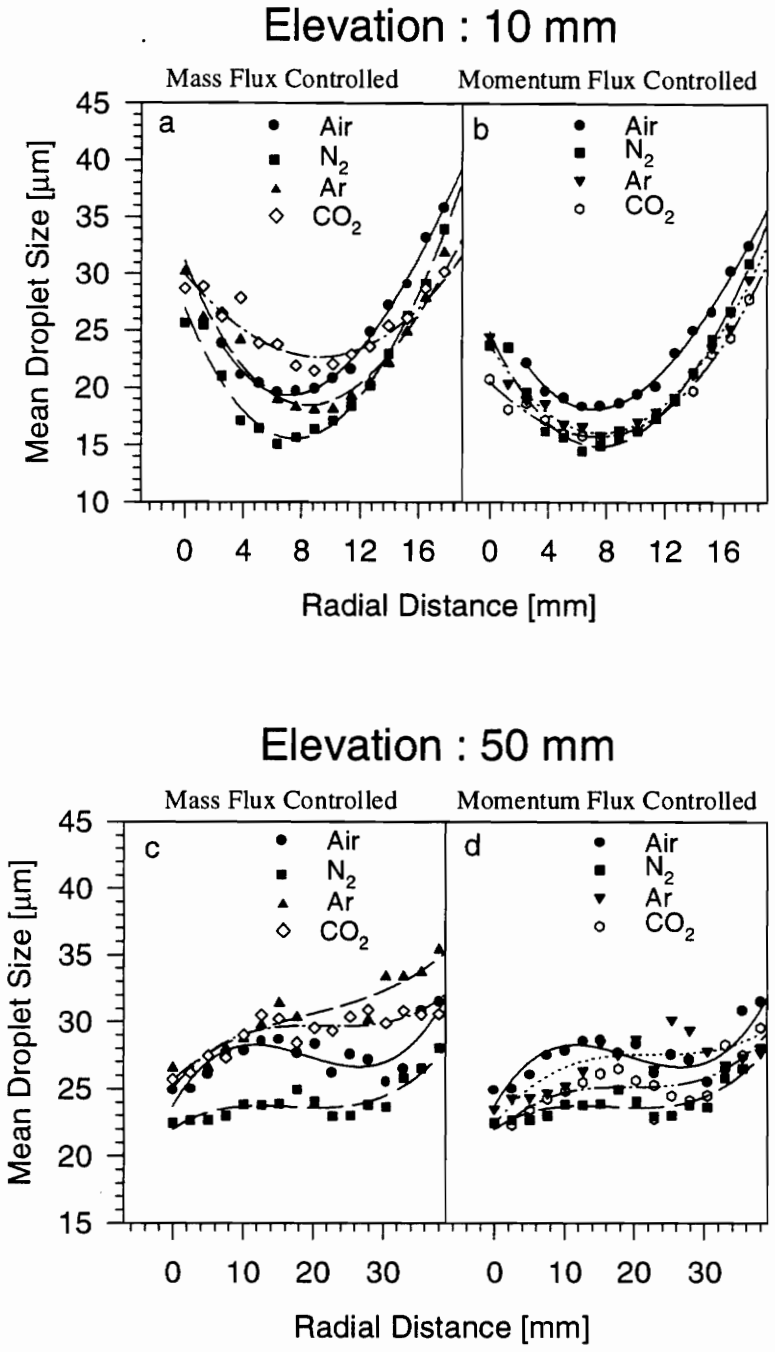

Figure 3.11: Sauter mean droplet size [µm] in burning sprays. (a) mass flow constant, z = 10 mm, (b) momentum flux constant, z = 10 mm, (c) mass flux constant, z = 50 mm, (d) momentum flux constant, z = 50 mm.

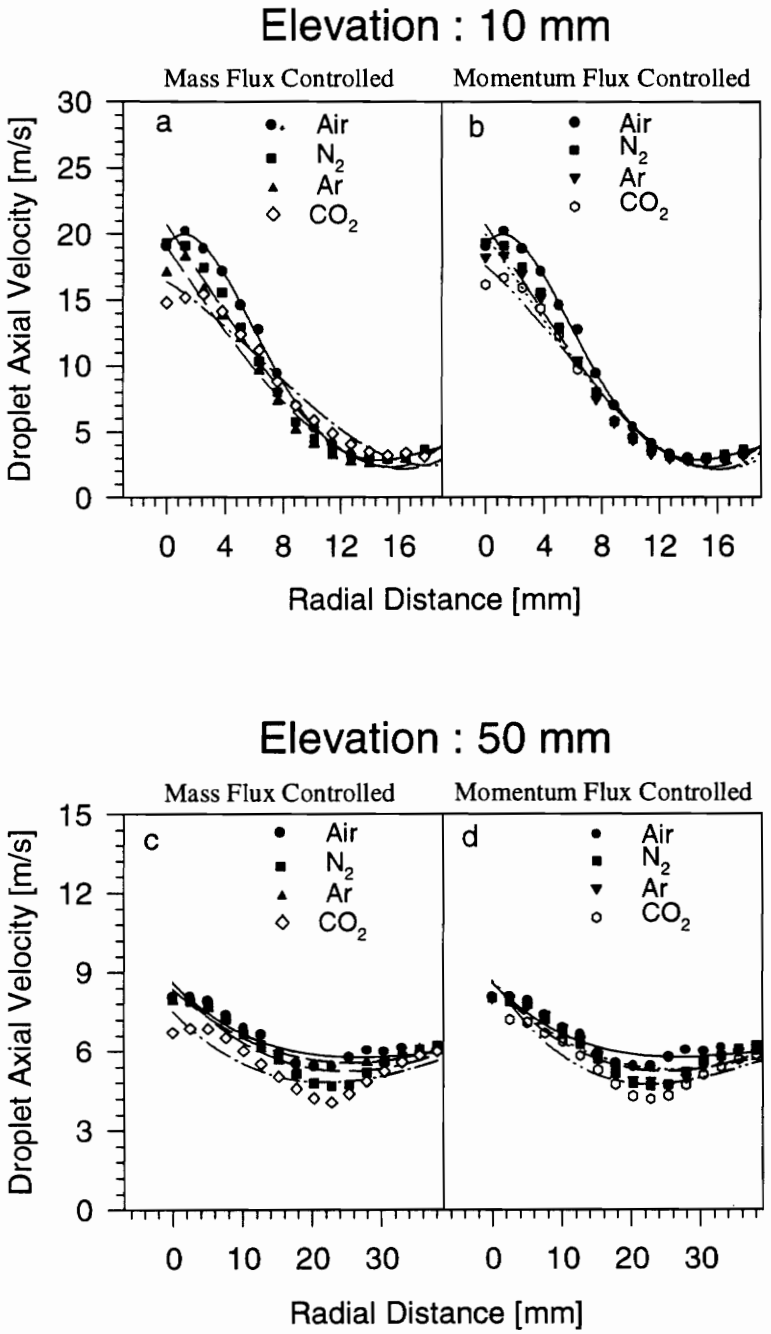

Figure 3.12: Axial droplet velocity [m/s] in burning sprays. (a) mass flow constant, z = 10 mm, (b) momentum flux constant, z = 10 mm, (c) mass flux constant, z = 50 mm, (d) momentum flux constant, z = 50 mm.

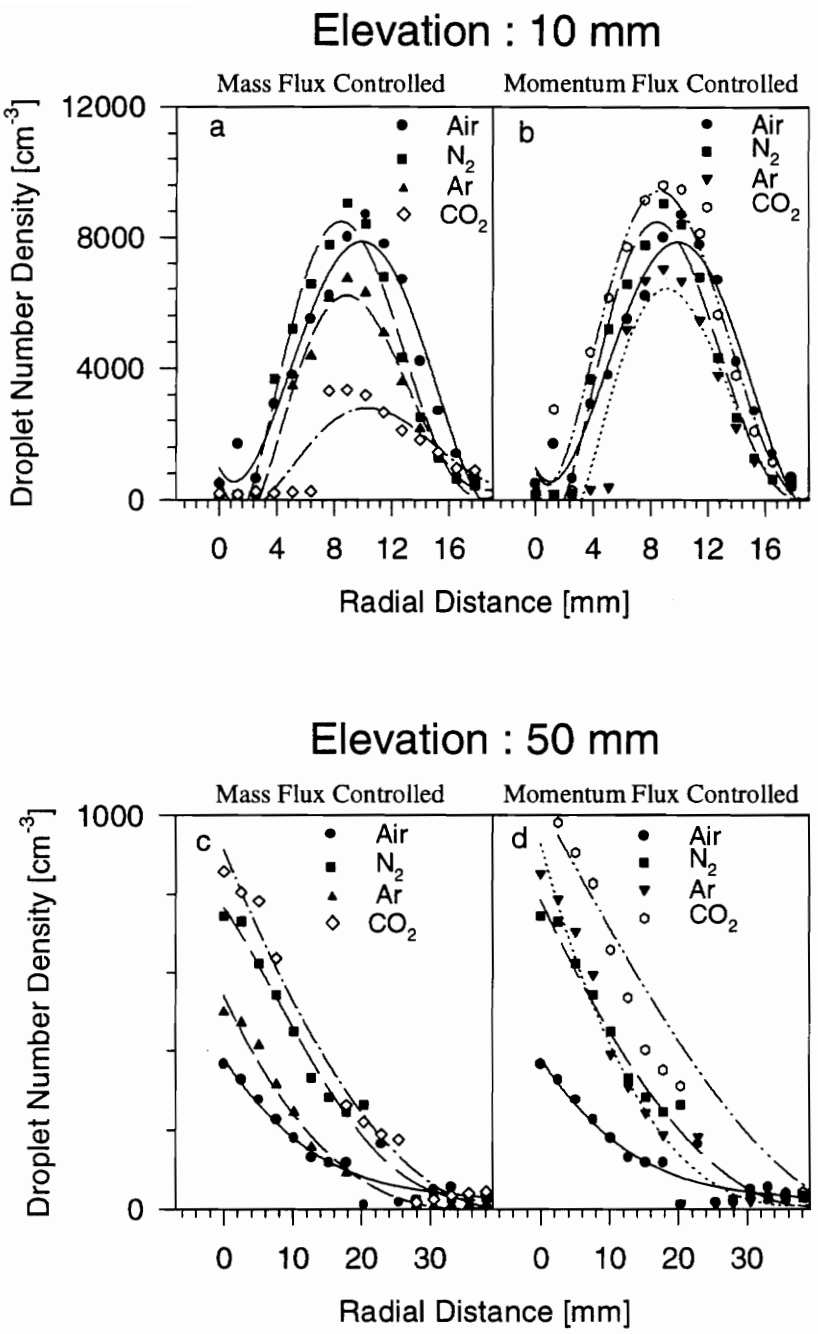

Figure 3.13: Droplet number density [Droplets/cm^3] in burning sprays. (a) mass flow constant, z = 10 mm, (b) momentum flux constant, z = 10 mm, (c) mass flux constant, z = 50 mm, (d) momentum flux constant, z = 50 mm.

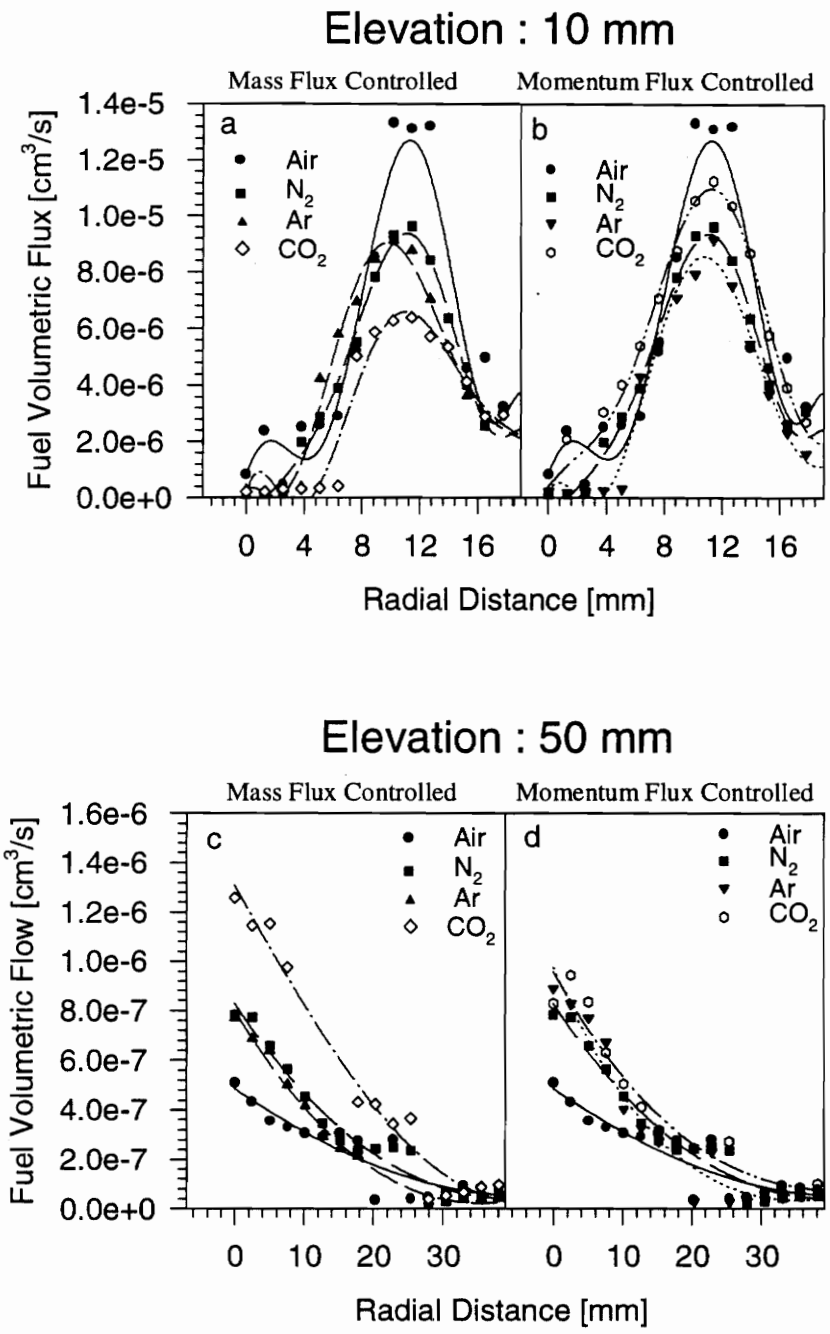

Figure 3.14: Fuel volumetric flux [cm^3/s] in burning sprays. (a) mass flow constant, z = 10 mm, (b) momentum flux constant, z = 10 mm, (c) mass flux constant, z = 50 mm, (d) momentum flux constant, z = 50 mm.

4.0 Discussion

General features in the burning and nonburning sprays were anticipated given the atomizer used. Droplet size increased and axial velocity decreased with increasing radial distance. At low elevations, droplet number density and fuel volumetric flow rate peaked at the spray boundary. At high elevations, these peaks occurred on the spray centerline. Changing the atomization gas flowrate from mass control to momentum control for the denser atomization gases (Ar and CO_2) resulted in smaller, faster droplets with higher number densities. All of these results were anticipated based on the results of previous research (Presser, et. al. 1988, Presser, et. al. 1989).

The empirical correlation by Wigg (1964) correctly predicted that the droplets produced in the mass controlled cases would be larger when denser atomization gases were used. Differences between Ar, CO_2 and N_2 were greatest in the central core of the spray, where the atomizing gas had the most effect on droplet behavior. Ar and CO_2 atomized droplets were larger than those atomized with air or N_2 (see Fig 3.7.b,d, and 3.11.b,d). At greater radial positions, the differences became much smaller, demonstrating that the atomizing gas had little effect on the noncombusting droplets once they moved off the spray centerline.

N_2 possesses a density and specific heat similar to air, but lacks oxygen. Therefore, the droplets in the nonburning N_2-assisted case have almost the same size (Fig. 3.7) and velocity (Fig 3.8) as the air-atomized droplets. In the burning case, the situation changed. Droplets formed by N_2 assist were clearly much smaller (Fig. 3.11) and slower (Fig. 3.12) near the spray boundary, where the majority of the fuel was present (Fig. 3.14). Taken together with the number density data presented in Fig. 3.13, it can be seen that at z = 10 mm, the N_2 assisted sprays have a similar number density of smaller droplets than the

corresponding air-atomized flame, resulting in an overall lower fuel flux rate (Fig. 3.14). At z = 50 mm, the trend reverses, and N_2 atomized droplets are smaller, and have a higher number density. Both N_2 and air have nearly identical physical characteristics, leaving the presence of oxygen in the air as the only explanation for this behavior. The droplets in the air assisted case, in fact, evaporate and combust at very low elevations. This presents an overall larger droplet size in this region of the spray, as smaller droplets are vaporized and disappear, lowering the number density and raising the mean droplet diameter. Confirmation of this may be seen in the velocity data presented in Fig. 3.8, where the droplet velocities at z = 10 mm are clearly significantly higher than the N_2 case, due to the effect of combustion on the droplets. N_2 produces a higher density of droplets at z = 50 mm because not as many droplets have combusted, and their overall size is smaller because few of the droplets have vaporized. Number densities at z = 50 mm are highest at the spray centerline due to the solid cone nature of the spray.

Both Ar and CO_2 generally produced larger droplets everywhere in the spray, regardless of whether the flow rate of atomizer was held mass or momentum constant, with CO_2 generally producing larger droplets than Ar. As in the case with N_2, there is no O_2 present in the atomizing gas to combust the droplets, and due to the higher densities and specific heats of CO_2 and Ar, the droplets at greater axial distance are substantially larger than in the N_2 case. Comparing the mass and momentum controlled cases, it is clear that the momentum controlled cases are significantly better atomized - droplet sizes are significantly smaller (Figs. 3.7 and 3.11), and the number density of droplets is greater (Fig. 3.9 and 3.13). This effect is due to the greater energy imparted to the liquid fuel by the momentum controlled atomizing gas.

Some overall effects can be noted in comparing the burning and nonburning data. Droplet velocities are naturally higher in the burning sprays, due to the large relative velocity and lack of deceleration as a result of combustion (Gupta, in press). These differences become less significant at greater axial or radial distances, where the effect of combustion is not as great as the effect of the surrounding combustion gas on the droplet velocity. Nevertheless, significant differences between burning and nonburning cases remain. Droplet sizes in the lower central core of the spray are similar in both the combusting and nonburning sprays. As the droplets move upward and off-axis, the droplets become much smaller in the combusting cases, as they rapidly evaporate and burn. In the nonburning cases, the droplets evaporate more slowly, and the droplet sizes remain large in the absence of any combustion. The effect of oxygen on droplet evaporation and combustion can be clearly seen when comparing number densities in the nonburning (Fig. 3.9) and burning (Fig. 3.13) sprays, where droplet number densities at z = 50 mm are reduced 50 to 75% in the burning case compared to the nonburning case, whereas the droplet number densities at z = 10 mm are similar in both cases.

5.0 Conclusions

It has been shown that the substitution of air in an air-assist nozzle with other gases results in significant differences in droplet size, velocity, number density and fuel flux. Observations of the spray flames confirmed experimental findings, with larger, more luminous flames (for Ar and CO_2) containing larger, slower droplets than the shorter, less luminous flame obtained with air. Droplet size in both mass and momentum controlled cases increased with denser atomizing gases. In general, the denser gases examined provided an overall larger droplet size and lower number density, and had a lower droplet velocity than the reference air assisted case. These differences can be consistently explained by the effect of O_2 in the atomizing air, which by assisting in combustion reduced the droplet sizes and increased their velocity. In nonburning sprays, the chemical role of O_2 in the atomizing air is eliminated, and the droplet characteristics for air and N_2 are similar. The results suggest that atomizing gases with lower densities or greater mole fractions of O_2 may produce sprays with lower mean droplet sizes when utilized on a constant momentum flux basis.

Although the volumetric flux of atomizing gas is less than 1% of the total oxidizer flow, these results suggest that O_2 present within the atomizing gas plays a significant role in droplet formation and combustion. Due to its availability in regions where droplets are forming, it may enhance mixing and partially premix with the fuel.

Phase-Doppler interferometry has proven itself to be a superficially straightforward way of obtaining size and velocity information from the droplets in a spray. In practice, the system is sensitive to alignment, input laser power, and software settings. With practice, it can be very reliable - the data obtained here were taken over a two week period, yet data points taken different weeks still agreed within

5% after making changes to the facility, such as nozzle changes. Nevertheless, limits on the system's ability to resolve velocity distributions with significant positive and negative components made data collection in this swirling flow challenging.

Experiments are underway to elucidate the role of O_2 enrichment within the atomizing gas. This will be done through a combination of gas sampling and FTIR analysis, as well as temperature measurements throughout the spray. Mixtures of air enriched with oxygen (up to 40 mol %) will also be tested.

Anticipated future work includes the use of Laser Induced Incandescence (LII) to determine soot volume fraction within the combusting sprays. LII operates under the principle of incinerating the soot particles so that they radiate as they burn. The light given off by the particles as they burn is captured by an ICCD camera and recorded. Through spectral analysis of this signal, the local soot volume fraction may be determined. Equipment needed for this experiment include a doubled YAG laser operating at 534 nm, an ICCD camera, and various optical components to form the pulse laser energy into a sheet focused through the center of the fuel spray.

Planar laser induced fluorescence (PLIF) will also be applied to the burning sprays to obtain quantitative measurement of intermediate species of interest. Specifically, it is anticipated that OH and NO will be measured in the combusting sprays, which could further elucidate the effect of oxygen within the atomization air on the combustion characteristics of the spray.

References

Bachalo, W.D., Houser, M.J., Optical Engineering, Vol.23 No. 5, p. 583 (1984).

Bulzan, D.L., in SPIE - The International Society for Optical Engineering (L.C. Liou, ed.), Vol. 1862, pp. 113-122, (1993).

Durst, F., and Zarð, M. Proceedings LDA Symposium, Copenhagen, Denmark, p. 403 (1975).

Edwards, C.F. and Rudoff, R.C. Twenty-Third Symposium (International) on Combustion, The Combustion Institute, Pittsburgh, pp. 1353-1359 (1990).

Glantschnig, W.J. and Chen, S., Applied Optics Vol. 20 p. 2499 (1981).

Gupta, A.K., Lilley, D.G. and Syred, N., Swirl Flows, Abacus Press, Kent (1984).

Gupta, A.K., Presser, C., Hodges, J.T., and Avedisian, C.T., Journal of Propulsion and Power, vol. 12, num. 2, 1996 (in press).

Lefebvre, A.H. Atomization and Sprays, Hemisphere Publishing Co., (1989).

Presser, C., Gupta, A.K., and Semerjian, H.G.: Heat Transfer in Combustion Systems, ASME Winter Annual Meeting, Chicago, IL (1988).

Presser, C., Gupta, A.K., and Semerjian, H.G.: Heat Transfer in Combustion Systems, ASME Winter Annual Meeting, San Francisco, CA pp. 21-34 (1989).

Presser, C., Gupta, A.K., and Semerjian, H.G.: Combust. Flame 92:25-44 (1993).

Presser, C., Gupta, A.K., Semerjian, H.G., and Avedisian, C.T.: Journal of Propulsion and Power, Vol. 10, num. 5, pp. 631-638 (1994).

Presser, C., Gupta, A.K., Avedisian, C.T., and Semerjian, H.G.: Atomization and Sprays, Vol. 4, pp. 207-222, (1994).

van de Hulst, H.C., Light Scattering by Small Particles, Wiley, New York (1957).

Wigg, L.D.: Drop-Size Predictions for Twin Fluid Atomizers, J. Inst. Fuel, Vol. 27, pp. 500-505 (1964).

Appendix A: Common Definitions and Notations

A. 1. Common Averages

The following definitions are given for the most frequently used mean and median diameters:

Arithmetic Mean Diameter	D_{10}	:	The average of the diameters of all the droplets in the spray sample.
Surface Mean Diameter	D_{20}	:	The diameter of a droplet whose surface area, if multiplied by the total number of droplets, will equal the surface area of the sample.
Volume Mean Diameter	D_{30}	:	The diameter of a droplet whose volume, if multiplied by the total number of droplets, will equal the total volume sample.
Sauter Mean Diameter	D_{32}	:	The diameter of a droplet whose ratio of volume to surface area is equal to that of the complete spray sample.
Mass Mean Diameter	D_{43}	:	The diameter of a droplet whose ratio of the diameter power 4 to the diameter power 3 is equal to that of the complete spray sample.

Of these diameter definitions, mass mean diameter is the largest, and arithmetic mean the smallest. Sauter Mean diameter will frequently be about 80% of the mass mean diameter.

Using the notations D_k, D_k^2, D_k^3 to indicate powers of the diameters in the k^{th} bin and N as the number of drops in the sample, these quantities are found from:

a. Arithmetic Mean Diameter: $$D_{10} = \sum_k \frac{D_k}{N} \quad \text{(A.1)}$$

b. Surface Mean Diameter: $$D_{20} = \left[\sum_k \frac{D_k^2}{N} \right]^{\frac{1}{2}} \quad \text{(A.2)}$$

c. Volume Mean Diameter: $$D_{30} = \left[\sum_k \frac{D_k^3}{N} \right]^{\frac{1}{3}} \quad \text{(A.3)}$$

d. Sauter Mean Diameter: $$D_{32} = \frac{\sum_k D_k^3}{\sum_k D_k^2} \quad \text{(A.4)}$$

e. Mass Mean Diameter: $$D_{43} = \frac{\sum_k D_k^4}{\sum_k D_k^3} \quad \text{(A.5)}$$

f. Arithmetic Mean Velocities: $$v_{mean} = \sum_k \frac{v_k}{N} \quad \text{(A.6)}$$

(were v can also be u)

g. Standard Deviation: $$\sigma = \sqrt{\frac{\sum x^2 - \frac{\left(\sum x\right)^2}{N}}{N-1}} \quad \text{(A.7)}$$

h. Root mean square: $$rms = \frac{\sum \left[\left(\sqrt{x_i - x_{mean}} \right)^2 \right]}{N} \quad \text{(A.8)}$$

(were x can be radial velocity, axial velocity or diameter of the droplets for g. and h.)

A.2 Swirl Number

The swirl number was determined according to the method outlined by A. K. Gupta et al.(1984) and is determined from:

$$S = \frac{\sigma \cdot d}{2B} \cdot \left[1 - \left(\frac{rh}{d}\right)^2\right] \qquad (A.9)$$

where

$$\sigma = \frac{\tan\alpha}{(1-\Psi)\cdot\left[1+\tan\alpha\cdot\tan(\pi/z)\right]} \qquad (A.10)$$

$$\Psi = \frac{2T}{2\cdot\pi\cdot RI\cdot\cos\alpha} \qquad (A.11)$$

and z = number of vanes,

T = vane thickness,

B = vane height,

RI = distance from burner axis to vane,

d = outer diameter of exit duct,

rh = inner diameter of exit duct.

Example calculation:

z = 12

T = 0.125

B = 2

RI = 2.5

d = 2

rh = 0.75

α = 40°

$$\Psi = \frac{0.125}{\pi \cdot 2.5 \cdot \cos 40^\circ} = 0.02078 \qquad \text{(A.12)}$$

$$\sigma = \frac{\tan 40^\circ}{(1 - 0.02078) \cdot \left[1 + \tan 40^\circ \cdot \tan(\pi/12)\right]} = 0.6996 \qquad \text{(A.13)}$$

$$S = \frac{0.6696 \cdot 2}{2 \cdot 2} \cdot \left[1 - \left(\frac{0.75}{2}\right)^2\right] = 0.3 \qquad \text{(A.14)}$$

A.3 Equivalence Ratio

The equivalence ratio is given as:

$$\varphi = \frac{\left(\frac{m_f}{m_a}\right)_{actual}}{\left(\frac{m_f}{m_a}\right)_{stoichiometric}} \qquad \text{(A.15)}$$

where m_f = mass of the fuel,

m_a = mass of the air.

Example calculation:

$$O_{min} = \frac{C}{12} + \frac{H}{4} + \frac{S}{32} \quad \left[\frac{kmol \quad O}{kg \quad fuel}\right] \qquad \text{(A.16)}$$

$$Air_{min} = \frac{O_{min}}{0.21} \quad \left[\frac{kmol \quad Air}{kg \quad fuel}\right] \qquad \text{(A.17)}$$

$$Air_{min} = \frac{O_{min}}{0.21} \cdot M_{Air} \left[\frac{kg\ \ Air}{kg\ \ fuel}\right] \tag{A.18}$$

where:

O_{min} = Oxygen minimum needed for the complete reaction of the fuel,

Air_{min} = Air minimum needed for the complete reaction of the fuel,

C = mass fraction carbon in the fuel

H = mass fraction hydrogen in the fuel

S = mass fraction sulfur in the fuel

M_{Air} = molar mass of the air.

$$O_{min} = \frac{0.8651}{12} + \frac{0.1392}{4} + \frac{0.00018}{32} = 0.1068 \left[\frac{kmol\ \ O}{kg\ \ fuel}\right] \tag{A.19}$$

$$Air_{min} = \frac{0.1068}{0.21} \cdot 28.963 = 14.742 \left[\frac{kg\ \ Air}{kg\ \ fuel}\right] \tag{A.20}$$

$$\left(\frac{m_f}{m_a}\right)_{stoichiometric} = (Air_{min})^{-1} = 0.06783$$

$$\varphi = \frac{\left(\frac{4.104}{210}\right)}{0.067833} = 0.28782 \tag{A.21}$$

(The numbers used in these calculations are based on a chemical analysis of the fuel by Penniman and Browne, Inc., Chemists-Engineers-Inspectors, 6252 Falls Road, Baltimore, MD 21209. Analysis results showed the fuel to contain the following: carbon = 86.51%, hydrogen = 13.92%, nitrogen = 0.01% and sulfur = 0.018% on a mass basis.)

A.4 Experimental Conditions

For all experiments reported in this work, the following experimental conditions were:

Fuel flow rate: 4.1 kg/h

Atomization gas flow rate (mass flow controlled): 1.64 kg/h

Atomization gas flow rate (momentum flow controlled): 7.86×10^{-2} kg/m·h^2 (at the rotometer)

Main combustion air flow rate: 161.4 m^3/h

Swirl vane angle/ Swirl number: 40° / 0.3

A.5 Wigg Size Correlation for Internal Mixing Air-Assist Atomizers

Given an air-assist atomizer and a single fuel (or liquid), the variation of mass mean droplet diameter with atomization gas flow rate and properties may be expressed as:

$$MMD \propto \left(1 + \frac{\dot{m}_L}{\dot{m}_A}\right)^{0.5} \rho_A^{-0.3} U_R^{-1.0} \qquad \text{(A.22)}$$

Where m indicates mass flow rate, ρ density, U_R the relative velocity of the atomization gas and the fuel, which is taken here to just be a function of atomization gas velocity, since $U_A >> U_F$.

Assume two different atomization gases, 1 and 2, where:

$$\rho_1 = 2\rho_2 \qquad \text{(A.23)}$$

in order to maintain a constant mass flux of atomization gas (ρU), the velocity of gas 1 would have to be half that of gas 2. Therefore:

$$\frac{MMD_1}{MMD_2} \propto \frac{\left(1+\frac{\dot{m}_L}{\dot{m}_1}\right)^{0.5} \rho_1^{-0.3} U_1^{-1.0}}{\left(1+\frac{\dot{m}_L}{\dot{m}_2}\right)^{0.5} \rho_2^{-0.3} U_2^{-1.0}} \tag{A.24}$$

Since $m_1 = m_2$, this expression can be simplified. Substituting the relationship in eq. A.23 into eq. A.24:

$$\frac{MMD_1}{MMD_2} \propto \frac{(2\rho_2)^{-0.3}}{\rho_2^{-0.3}} \frac{2U_2}{U_2} \tag{A.25}$$

simplifying:

$$\frac{MMD_1}{MMD_2} \propto 1.63 \tag{A.26}$$

Therefore, if the density of the atomization gas is doubled, the mass mean droplet size will increase by 63% according to this correlation. In tests with nitrogen and carbon dioxide, sauter mean size differences on the order of 50% were measured on the spray centerline, whereas carbon dioxide is 57% more dense than nitrogen.

In the case where the momentum flux is maintained constant, ρU^2 is constant. For the same gases 1 and 2, we have the following:

$$\rho_1 U_1^2 = \rho_2 U_2^2$$
$$U_1 = \frac{\sqrt{2}U_2}{2} \tag{A.27}$$

$$\frac{MMD_1}{MMD_2} \propto \frac{\left(1+\frac{\dot{m}_L}{\dot{m}_1}\right)^{0.5}}{\left(1+\frac{\dot{m}_L}{\dot{m}_2}\right)^{0.5}} \bullet \frac{\rho_1^{-0.3}}{\rho_2^{-0.3}} \bullet \frac{U_1^{-1.0}}{U_2^{-1.0}} \tag{A.28}$$

taking the typical values used for flow rate in this study (4.1 kg/h fuel, 1.64 kg/h for air, assumed to be gas 1) and substituting:

$$\frac{MMD_1}{MMD_2} \propto \frac{\left(1+\frac{4.1\,kg/h}{\sqrt{2}\cdot 1.64\,kg/h}\right)^{0.5}}{\left(1+\frac{4.1\,kg/h}{1.64\,kg/h}\right)^{0.5}} \bullet \frac{(2\rho_2)^{-0.3}}{\rho_2^{-0.3}} \bullet \sqrt{2} \qquad \text{(A.29)}$$

$$\frac{MMD_1}{MMD_2} \propto 1.0211 \qquad \text{(A.30)}$$

Therefore, if the momentum flux of the atomization gases are maintained constant, the mass mean droplet size will also remain nearly constant regardless of the atomization gas density.

A.6 Spray Angle

The spray angle is defined as the angle between the velocity vector of an individual droplet and the centerline.

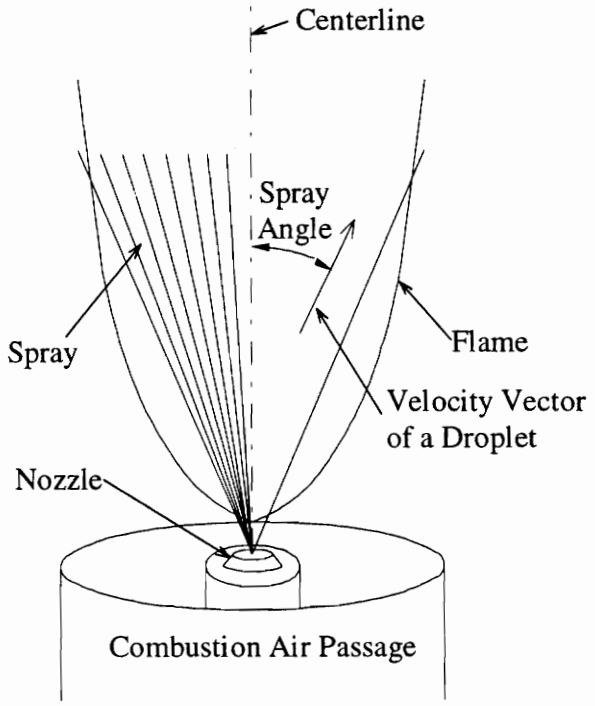

Figure A.1: Definition of the spray angle

Appendix B - Principals of Phase-Doppler Interfereometry

The following technical development of the principals of phase-Doppler interferometry is based on the development of Bachalo, et. al. (1984). Dr. Bachalo and his colleagues at Aerometrics did much of the initial development on the principals and operation of this system in the early 1980's.

The scattering of light by homogeneous dielectric spheres (in this case, droplets) larger than the light wavelength and with refractive indices sufficiently different than the surrounding medium may be approximated by Mie theory (van de Hulst, 1957).

A beam of light scattered by diffraction through a droplet, may be approximated by the function:

$$S_{diff}(\alpha,\theta) = \alpha^2\left[\frac{J_1(\alpha \sin\theta)}{\alpha \sin\theta}\right] \qquad \text{(B.1)}$$

where J_1 is the Bessel function, $\alpha = \pi d/\lambda$, and θ is the scattering angle. This forward-scattered light becomes more intense as a function of the droplet diameter squared, and has a smaller angular distribution as droplet size is reduced. For droplets of size with $\alpha >$ 15, diffraction becomes insignificant at scattering angles greater than 10°. Diffraction can therefore be avoided by careful selection of light wavelength and proper placement of the receiving optics.

When a ray of light impinges on a transparent droplet, it reflects and/or refracts through it according to the laws of simple geometric optics (see Fig. B.1). According to Snell's law, the direction of the refracted ray is given by:

$$\cos\tau = m\cos\tau' \qquad \text{(B.2)}$$

where τ and τ' are the angles between the surface tangent and the incident and refracted rays, respectively. The emerging rays are characterized by two parameters: the angle τ of the incident ray and the integer p of the interface from which it emerges - p = 0 for the first surface reflection, p = 1 for the first transmitted ray, and p = 2 for the ray emerging after one internal reflection. The angle between the incident and p*th* ray is given by:

$$\theta = 2(p\tau' - \tau)$$

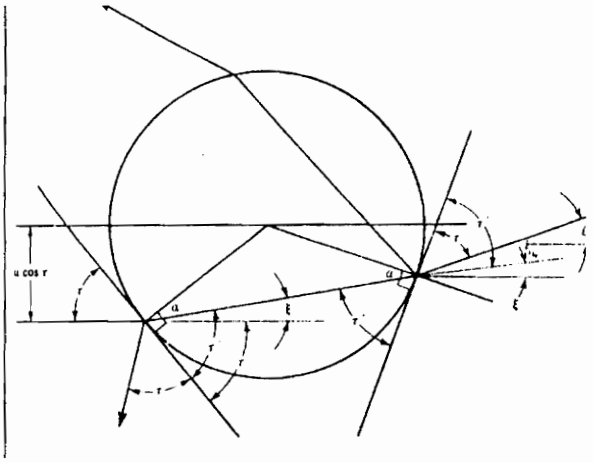

Figure B.1: Geometrical diagram of light rays scattered by a sphere (Bachalo, 1984)

In van de Hulst's notation, the scattered light is described in terms of two amplitude functions, $S_1(\alpha, m, \theta)$ and $S_2(\alpha, m, \theta)$ for the perpendicular (to the scattering plane) and parallel incident polarizations, respectively. Since large spheres scatter most of the incident light in the forward direction, only the first two terms describing the rays emerging from the interfaces need to be considered.

Glantschig and Chen (1981) obtained the expressions for the amplitude function describing the rays reflected from the first surface of the sphere:

$$S_1^{(1)}(\alpha,m,\theta)=\alpha\frac{\sin\frac{\theta}{2}-\sqrt{m^2-\cos^2\frac{\theta}{2}}}{\sin\frac{\theta}{2}+\sqrt{m^2-\cos^2\frac{\theta}{2}}}\times\frac{1}{2}\exp\left[j\left(\frac{\pi}{2}+2\alpha\sin\frac{\theta}{2}\right)\right]$$

$$S_2^{(1)}(\alpha,m,\theta)=\alpha\frac{m^2\sin\frac{\theta}{2}-\sqrt{m^2-\cos^2\frac{\theta}{2}}}{m^2\sin\frac{\theta}{2}+\sqrt{m^2-\cos^2\frac{\theta}{2}}}\times\frac{1}{2}\exp\left[j\left(\frac{\pi}{2}+2\alpha\sin\frac{\theta}{2}\right)\right] \qquad \text{(B.3)}$$

where j is the imaginary value $j^2=-1$, superscript (1) implies the p=0 reflection, and subscripts 1 and 2 represent the perpendicular and parallel polarizations, respectively. The amplitude functions for the rays emerging from the second surface after refraction by the sphere are given by:

$$S_1^{(2)}(\alpha,m\theta)=\alpha\left[1-\left(\frac{1+m^2-2m\cos\frac{\theta}{2}}{1-m^2}\right)^2\right]\times\sqrt{\frac{m^2\sin\frac{\theta}{2}\left(m\cos\frac{\theta}{2}-1\right)\left(m-\cos\frac{\theta}{2}\right)}{2\sin\theta\left(1+m^2-2m\cos\frac{\theta}{2}\right)}}\times$$

$$\exp\left[j\left(\frac{3\pi}{2}-2\alpha\sqrt{1+m^2-2m\cos\frac{\theta}{2}}\right)\right],$$

$$S_2^{(2)}(\alpha,m\theta)=\alpha\left[1-\left(\frac{\left(1+m^2\right)\cos\frac{\theta}{2}-2m}{\left(m^2-1\right)\cos\frac{\theta}{2}}\right)^2\right]\times\sqrt{\frac{m^2\sin\frac{\theta}{2}\left(m\cos\frac{\theta}{2}-1\right)\left(m-\cos\frac{\theta}{2}\right)}{2\sin\theta\left(1+m^2-2m\cos\frac{\theta}{2}\right)^2}}\times$$

$$\exp\left[j\left(\frac{3\pi}{2}-2\alpha\sqrt{1+m^2-2m\cos\frac{\theta}{2}}\right)\right] \qquad \text{(B.4)}$$

Summing the amplitude functions yields the total forward scattering:

$$S_j(\alpha,m,\theta)=S_{diff}(\alpha,\theta)+S_j^{(1)}(\alpha,m,\theta)+S_j^{(2)}(\alpha,m,\theta) \qquad j=1,2. \qquad \text{(B.5)}$$

The dimensionless intensities i_j are:

$$i_j(\alpha, m, \theta) = \left|S_j(\alpha, m, \theta)\right|^2 \qquad \text{(B.6)}$$

With the exception of cases where the scattering occurs at grazing or near grazing incidence, these expressions provide accurate results, which have been shown to be accurate for water droplets down to 5μm.

For adequately sized droplets, the intensity of the scattered light may be used for size analysis. The square of the droplet diameter can be assumed to be proportional to the scattered light intensity:

$$I_{scat}(d, m, \theta) = C(m, \theta)d^2 \qquad \text{(B.7)}$$

where $C(m,\theta)$ is a constant.

Light rays emerging from a spherical particle will have different path lengths depending on the angle of scatter and the size of the sphere. The intensities of the outgoing beams can therefore not be added directly. The beams (having all originated from the same coherent source) must have their complex amplitudes added, and the squared modulus then becomes the correct intensity.

In order to compute these phases from ray optics, van de Hulst references the actual ray to a hypothetical ray scattered without a phase lag at the center of the sphere. Neglecting the phase shifts of π at the reflection and $\pi/2$ at the focal lines, a simple geometric analysis results in the following expression:

$$\eta = 2\alpha(\sin\tau - pm\sin\tau') \qquad \text{(B.8)}$$

for the phase shift with respect to the reference ray. It is of interest to note that this phase difference is directly proportional to α, suggesting a means of obtaining size information.

One approach for obtaining size information from the phase shift is to utilize a dual-beam scattering arrangement as used in 1-D laser Doppler velocimetry (see Fig. B.2). Assuming linearly polarized light, the amplitude functions associated with scattering from beams one and two are:

$$S_{11}(m,\theta,d) = \sqrt{i_1}\exp(j\sigma_1)$$

$$S_{12}(m,\theta,d) = \sqrt{i_2}\exp(j\sigma_2) \qquad \text{(B.9)}$$

where the double subscript indicates that only polarization 1 is considered and $\sigma = \eta$. When a spherical particle passes through the intersection of the beams, it will scatter light from each beam independently, i.e. as if the other beam were not present. Therefore, the scattered light intensity may be described as:

$$E_1(m,\theta,d) = S_{11}(m,\theta,d)\frac{\exp(-jkr + j\omega_1 t)}{jkr},$$

$$E_2(m,\theta,d) = S_{12}(m,\theta,d)\frac{\exp(-jkr + j\omega_2 t)}{jkr}, \qquad \text{(B.10)}$$

where $k = 2\pi/\lambda$ is the wave number and ω is the angular frequency. The total scatter is obtained by summing the complex amplitudes from each beam and then determining the intensity, which is

$$I(m,\theta,d) = \left(|E_1|^2 + |E_2|^2 + 2|E_1||E_2|\cos\sigma\right), \qquad \text{(B.11)}$$

where σ is the phase difference between the scattered fields. In this expression, the cross product term corresponds to the sinusoidal intensity variation of the fringe pattern, while the other terms are the pedestal components.

Since the rays from beams 1 and 2 intersect at a small angle γ (< 10°), the scattering angles θ_1 and θ_2 are approximately equal for those pairs of rays that reach a common point in space and interfere. The amplitude functions S_1 and S_2 are therefore also approximately equal, and the visibility of the fringe pattern is approximately unity. The spatial frequency

of the fringe pattern is determined by the relative phase difference σ of the interfering light waves scattered from beams 1 and 2. Figure B.3 is a photograph of the scattered light interference pattern.

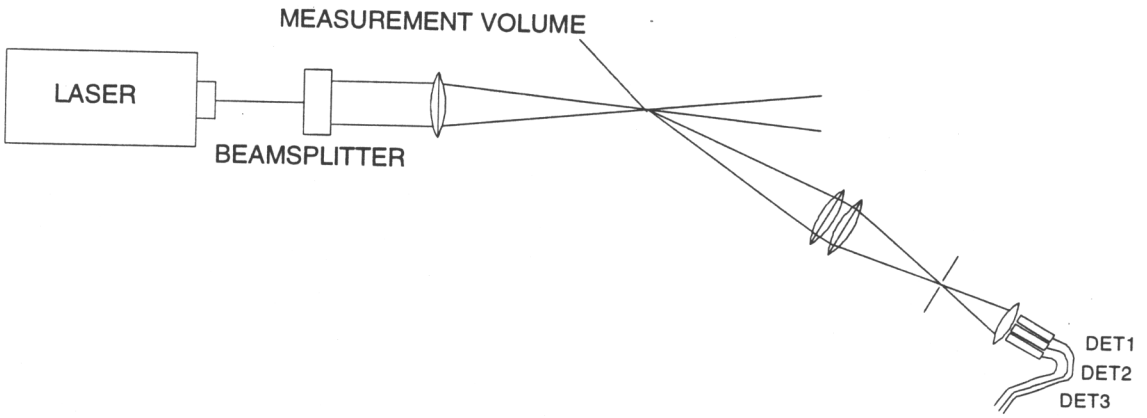

Figure B.2: Schematic of optical system for 1-D LDV and droplet sizing system.

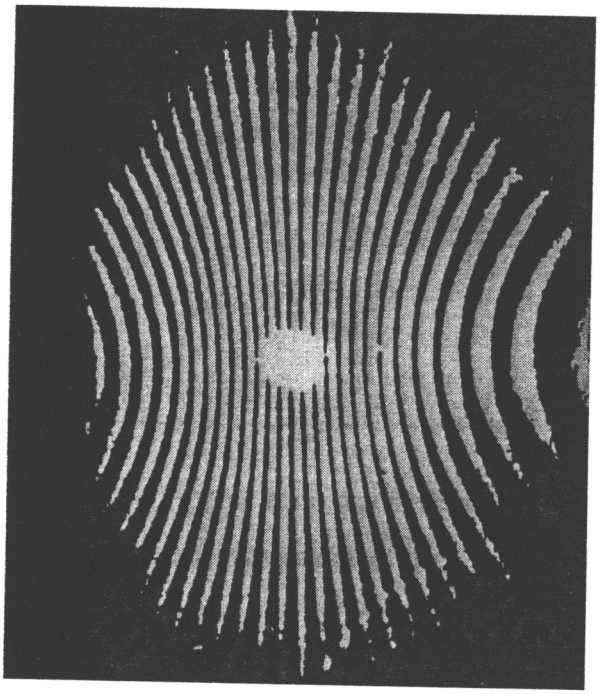

Figure B.3: Interference pattern produced by a droplet scattering laser light (Bachalo, et. al. 1984)

When a droplet moves through a pair of intersecting laser beams, the fringe pattern produced moves at the Doppler difference frequency, which is a function of the beam intersection angle, light wavelength, and velocity of the droplet. The spatial frequency of the fringe pattern is dependent on the angle of observation, droplet index of refraction, beam intersection angle, laser wavelength, and droplet diameter. Placement of a receiving optic to collect the scattered light will produce a Doppler burst signal, as shown in Fig. B.4. The lens functions in effect as a length scale, measuring the spatial frequency of the scattered fringe pattern. Integration of this pattern over the received aperture produces a Doppler burst signal which may be related to the droplet size.

Given the fact that the interference fringe pattern produced by the scattered light is related linearly to the droplet size, the mathematical description of the interference pattern can be derived as a straightforward geometry exercise. Each point in space may be associated with ray angles θ_1 and θ_2, which defines the amplitude and phase of each ray reaching the point. With the complete theoretical description of the fringe pattern produced by the scattered light, the drop size may be obtained from accurate measurement of the spatial frequency of the interference fringe pattern.

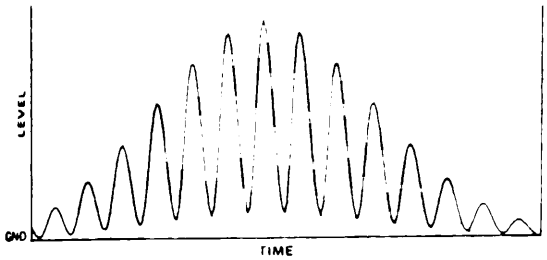

Figure B.4: Laser Doppler burst signal (Bachalo, et. al. 1984)

The scheme used to measure the spatial frequency of the scattered fringe pattern requires the use of two or more detectors separated by a fixed distance. As a droplet passes through the intersecting beams, the fringe pattern appears to move past the receiver at the Doppler difference frequency. A Doppler burst similar to that shown in Fig. B.4. will be produced by each detector, but with a phase shift between them, as shown in Fig. B.5.

The signals in Fig. B.5 have been high-pass filtered to remove the pedestal component shown in Fig. B.4. The phase shift is determined by measuring the time between the zero crossings of the signals from detectors 1 and 2 and dividing by the measured Doppler period:

$$\phi_{1-2} = \frac{\tau_{1-2}}{\tau_D} \times 360°, \qquad \text{(B.12)}$$

where the measurements are averaged over all the cycles in the Doppler burst. Measurements of the phase shift are then related to the droplet size using the computed linear relationships shown in Fig. B.6. In this figure, the abscissa is the drop size made dimensionless with delta, which is the fringe spacing assumed to be formed at the intersection of the two laser beams and is a function of the light wavelength and the laser beam intersection angle.

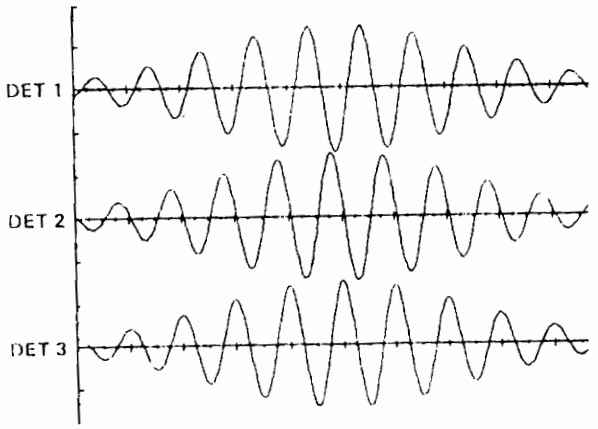

Figure B.5. High-pass filtered Doppler burst signals illustrating the phase shift between detectors (Bachalo, et. al. 1984).

In Fig. B.6., the effect of changing optical parameters including the beam intersection angle, collection angle, droplet index of refraction, laser wavelength and scattering component detected is simply to change the slopes of the linear response curves.

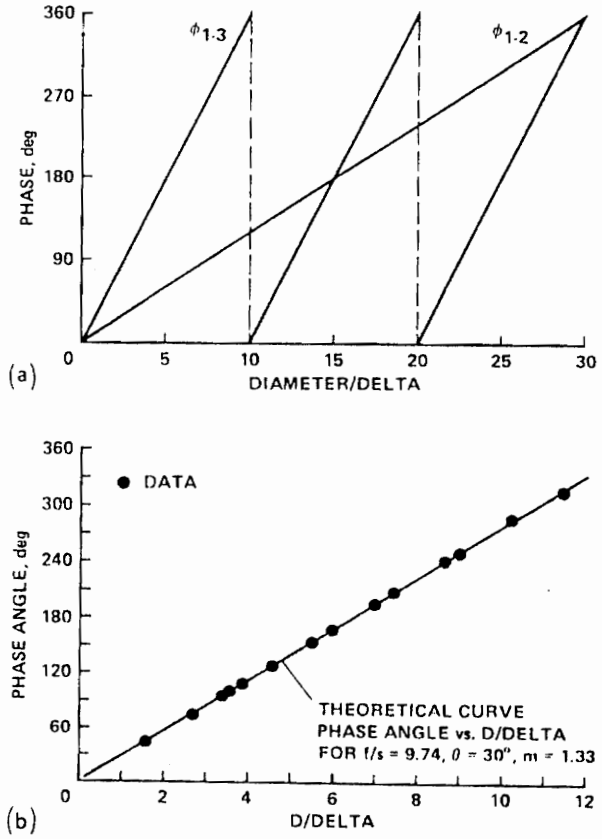

Figure B.6: Theoretical prediction of phase variation with dimensionless drop size. (a) relationship for three detectors and (b) comparisons with experiment (Bachalo, 1984).

Three detectors are required to ensure that no ambiguities in measurement occur. When measuring a polydisperse spray without prior knowledge of the size distribution, phase shifts of greater than 360° may occur. Without a third detector, such occurrences would be detected as being less than 360°. The third detector provides a logical test to identify and eliminate such uncertainties. By properly setting the spacing between the detectors, a wide range of size sensitivity may be obtained as shown on curves ϕ_{1-2} and ϕ_{1-3}. The two phase angles serve as a redundant measurement for verifying the data and extending the size range sensitivity at one optical setting by a factor of approximately 100. Since the droplets scatter light in proportion to their diameter squared, this would require a dynamic range of 10^5 or more in the detectors. However, detector gain may be easily reset to select optimum sensitivity for a given size class of droplet without any optical adjustments

or realignment. Figure B.6.b shows experimental verification of predicted instrument response, and was obtained using a monodisperse droplet generator.

Since the system uses two intersecting beams to produce a fringe pattern through which droplets pass, it can also be used as a velocimeter. In the present work, two pairs of intersecting beams were used, which made it possible to measure velocity in two directions. In addition, this provided an important check in the system. Droplet size was determined by each pair of beams, and cross-checked to ensure that identical sizes were determined by each phase delay. If the delays differed, it indicated that either an error had occurred, or the droplet was not spherical. In either case, the signal was rejected. Signals were also rejected if the detectors saturated due to excessive voltage on the PMTs, or if the droplet was not fully within the probe volume.

Figures B.7. and B.8. show the results of some of the calibration tests from Bachalo, et. al. (1984). In Fig. B.7., a comparison between the PDI measured drop size data and the manufacturer (Delavan) supplied drop-size distribution data is shown, and agrees with the manufacturer supplied data well.

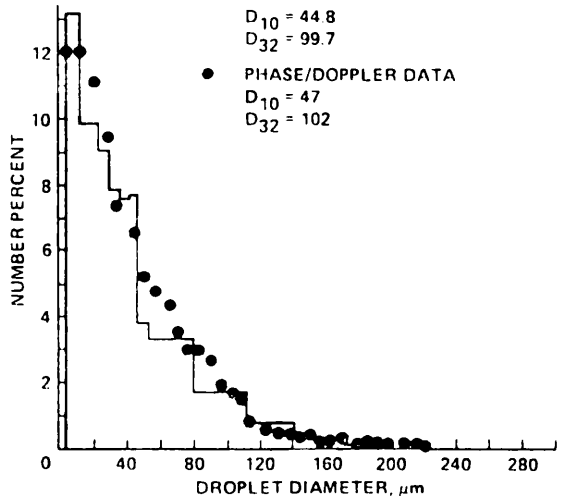

Figure B.7: Comparison with drop size distributions measured by Delavan pressure atomizer 45 B 0.6 gph at 60 psig water.

Figure B.8 shows the effects of instrument setup on PDI measured droplet size. A PDI system's sensitivity to droplets can be affected by operator input parameters. In the case shown here, it can be seen that changes in the droplet size range measured by the system can shift the size distribution detected by the system.

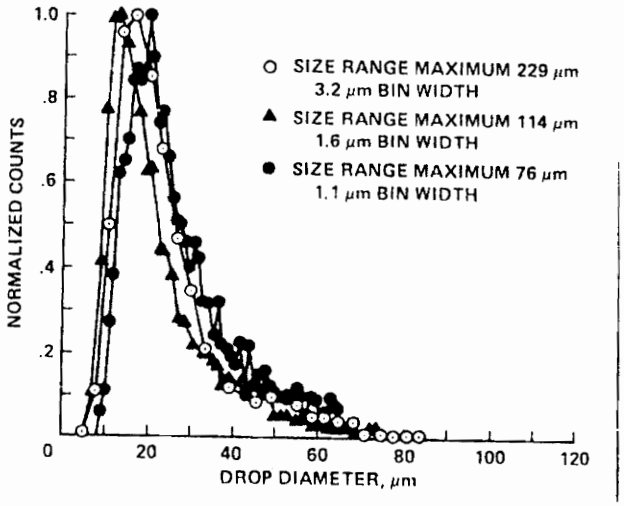

Figure B.8: Comparison of drop size distributions measured at three size range selections.

PDI systems are especially sensitive to the voltage settings on the detector PMTs. If these voltages are set too low, the PMTs will not be able to detect smaller droplets entering the control volume. The data collected will therefore be skewed towards the larger droplets. If the PMT voltages are set too high, larger droplets will saturate the PMTs, skewing the distributions towards smaller droplets.

In a 1994 paper by Presser, et. al. (1994), this topic was explored in detail. A mixture of dodecanol and methanol was used in a pressure jet atomizer. Two PMT voltage settings were utilized - in one case, the voltage were set so as to obtain a data rate of 200 Hz. Data rate is defined as the rate at which validated particles enter the control volume and are recorded. To become validated, the signals from these particles must achieve a sufficiently clean signal within the user defined bounds for size and velocity. The other

voltage was set so as to achieve optimum data rate, which was generally observed to occur with the PMTs saturated 1% of the time. This criterion is recommended by Aerometrics. In Fig. B.9., a strong effect on droplet size may be observed, where Sauter mean size drops from 58.3 to 46.3 μm, and axial velocity decreases from 19.3 to 14.2 m/s. This result was anticipated, since the voltages used in the low data rate case were lower than those used in the optimum gain case. In the 'B' portion of the Fig. B.9, the increased detection of smaller, slower particles is clearly shown.

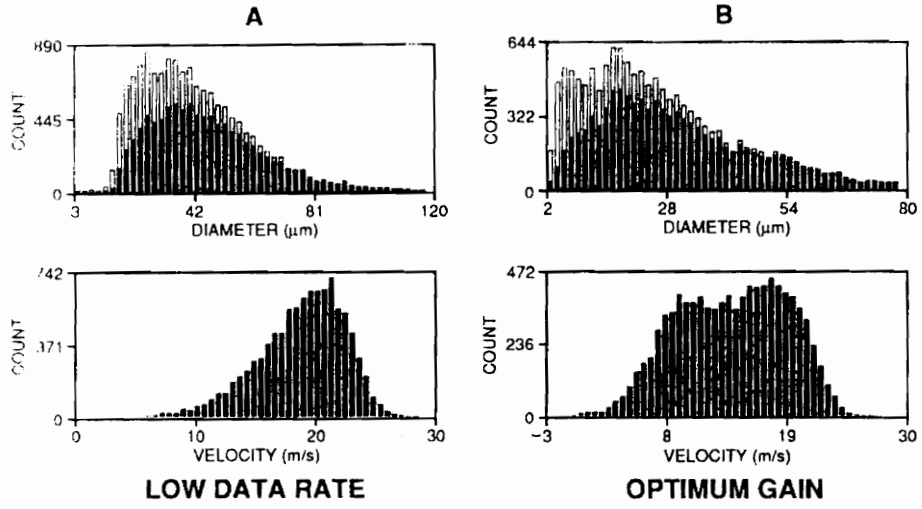

Figure B.9: Distribution of droplet size and velocity for the (A) low data rate and (B) optimum gain operating conditions of the phase Doppler system at r = 15.2 mm and z = 25.4 mm.

VITA

Robert Aftel was born June 8, 1968 in Queens, New York, where he lived until coming to Virginia Tech in 1991. In New York, he attended Stuyvesant High School, and then Cooper Union, which involved staying on the #6 train for exactly one more stop. At Cooper Union, he earned his bachelor's and master's degrees in mechanical engineering, under the mentorship of George Sidebotham, and met his wife, Nora Castro, who he married on July 16th, 1995 in the War Memorial Chapel at Virginia Tech. Robert's current plans are to get a good job and settle down.

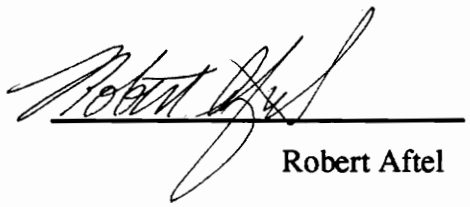

Robert Aftel